Title: The Heterochromatin protein 1 is a master regulator in RNA splicing precision deficient in ulcerative colitis

Jorge Mata-Garrido[1], Yao Xiang[1], Yunhua Chang-Marchand[1], Caroline Reisacher[1], Elisabeth Ageron-ardila[1], Chiara Guerrera[2], Inigo Casafont[3], Aurelia Bruneau[4], Claire Cherbuy[5], Xavier Treton[6], Anne Dumay[6], Eric Ogier-Denis[6], Eric Batsche[7], Mickael Costallat[7], Gwladys Revêchon[8], Maria Eriksson[8], Christian Muchardt[7] and Laurence Arbibe[1*]

[1]Department of Immunology, Infectiology and Hematology, Institut Necker-Enfants Malades (INEM), INSERM U1151, CNRS UMR 8253, Université Paris Descartes, Paris, France.
[2]Proteomic Platform Necker, PPN-3P5, Structure Fédérative de Recherche SFR Necker US24, 75015 Paris, France
[3]Grupo de Nanomedicina. Universidad de Cantabria-IDIVAL, Herrera Oria s/n, 39011, Santander, Spain
[4]National Institute for Agronomic Research (INRA), Unit on Ecology and Physiology of the Digestive Tract (UEPSD), 78352, Jouy-en-Josas Cedex, France
[5]Institut National de la Recherche Agronomique (INRA), MICALIS, UMR, Pôle Ecosystèmes, Jouy-en-Josas, France
[6]APHP/INSERM UMR 1149, équipe inflammation Intestinale UFR de Médecine, Xavier Bichat Université de Paris
[7]Institut de Biologie Paris-Seine, Sorbonne Université, CNRS UMR 8256, Biological Adaptation and Aging, Paris, France Paris, France
[8]Dept of Biosciences and Nutrition, Karolinska Institutet, SE-141 57 Huddinge, Sweden.

*Corresponding author: laurence.arbibe@inserm.fr

Abstract

Defects in RNA splicing have been linked to numerous human disorders, but remain poorly explored in inflammatory bowel disease (IBD). Here, we report that, in the gut epithelium of patients with ulcerative colitis (UC), the expression of the chromatin and alternative splicing regulator HP1γ is strongly reduced. Accordingly, inactivation of the HP1γ gene in the mouse gut triggered several IBD-like traits, including inflammation and dysbiosis. In parallel, we discovered that its loss of function broadly increased splicing noise, reducing requirement for canonical splicing consensus sequences, and favoring the usage of cryptic splice sites at numerous genes with key functions in gut biology. This notably resulted in the production of progerin, a noncanonical toxic splice variant of prelamin A mRNA, responsible for the Hutchinson Gilford Progeria Syndrome (HGPS) of premature aging. Likewise, production of progerin transcript was found to be a signature of colonic cells from UC patients. Thus, our study identifies HP1γ as a regulator of RNA metabolism *in vivo,* providing a unique mechanism linking anti-inflammation and accuracy of RNA splicing in the gut epithelium. HP1 defect may confer a general disturbance in RNA splicing precision to scrutinize in IBD and more generally in accelerating aging diseases.

Main

Inflammatory bowel disease (IBD), including ulcerative colitis (UC) and Crohn's disease (CD), are chronic inflammatory gut disorders characterized by an uncontrolled inflammation leading to bowel damage. While susceptibility gene loci have been identified, genetic factors account for only a portion of overall disease variance, indicating a need to better explore gene-environmental factor interactions in the development of the disease[1]. Epigenetics captures environmental stresses and translate them into specific gene expression pattern and little is known on the role played by chromatin deregulations in the pathogenesis of IBD. The Heterochromatin Protein 1 proteins (HP1α, HP1β, and HP1γ in mouse and human) are readers of the H3K9me2/3 histone modifications. They play key roles in formation and maintenance of heterochromatin, thereby participating in transcriptional gene silencing[2]. In addition to their "caretaker" function in heterochromatin, HP1 proteins display RNA binding activity described across the species[3]. In mammals, *in vitro* studies have shown that HP1γ binds intronic repetitive motifs of pre-messenger RNA[4] and promote co-transcriptional RNA processing as well as alternative splicing[5-6]. These studies suggest a role in RNA metabolism homeostasis that remains unexplored in intestinal disorders, in sharp contrast to neurodegenerative, cardiac or premature aging diseases[7]. In this study, we have delineated essential functions played by HP1γ in the regulation of gut homeostasis with relevance to IBD, and identify an essential safeguarding function on RNA splicing in the epithelium.

HP1γ inactivation triggers IBD-like traits

Our previously reported observations on the impact of HP1γ on the control of inflammation in the gut in response to bacterial infection[8] prompted us to examine expression of this protein in the context of chronic inflammation. To that end, we examined an available cohort of colonic biopsies in non-inflamed tissue from UC patients and from healthy individuals undergoing screening colonoscopies (**Figure 1a and Supplementary Data Table 1 for detailed description of the population).** Quantitative immunofluorescence (IF) showed a strongly decreased expression of HP1γ in the colonic epithelium of UC patients, as compared to healthy individuals (control patients) (**Figure 1a-b)**. Compromised HP1γ expression in association with UC was confirmed using the EXCY2 mouse model, which combines immune dysfunction (IL-10 deficiency) and epithelium NADPH oxidase 1 (Nox1) deficiency[9]. At early stage, these mice exhibited a spontaneous chronic colitis that evolved into a colitis-associated dysplasia and adenocarcinomas. Reduced HP1γ expression in the epithelium prevailed at the initial chronic inflammatory stage (1—5 months aged), while at the cancer stage, the expression was recovered, in coherence with the reported increase detection of the Cbx-protein family members in various cancers[10-11] (**Figure 1c-d**).

These observations, suggesting a role for HP1γ in chronic inflammation, prompted us to generate a Villin-creERT2:*Cbx3-/-* mouse model (referred to as *Cbx3* KO mice), allowing inducible inactivation of HP1γ in the epithelial lineage of the gut.

In these mice, tamoxifen gavage resulted in complete depletion in the HP1γ protein in the epithelium of the tested tissues, although the depletion was accompanied by an up-regulation of the HP1α and HP1β isoforms (**Extended data Figure 1**), as previously reported[12]. Next-generation RNA-sequencing on purified epithelial cells from either crypts, villi, and colon in young adult mice (8-10 weeks aged) indicated extensive changes in the transcriptome landscape in the *Cbx3* KO mice epithelium, with increased signature scores in pathways involved in lipid oxidation, symptomatic of oxidative damage (**Supplementary Data Table 2)**. Moreover, specifically in the colon, we noted a substantial increase in inflammatory gene expression confirmed by Q-PCR (**Figures 1e-f, Supplementary Data Table 2)**.

As both modified lipid metabolism and inflammation are conducive of gut microbiome dysbiosis[13], we further characterized the fecal microbiomes in mice (n=6 males and n=8 females) *via* Illumina sequencing of the V3-V4 region of bacterial 16S rRNA. In subsequent UniFrac principal coordinates analysis, *Cbx3* KO mice clustered away from the WTs, indicative of a shift in the microbial communities (**Figure 1g** and **Supplementary data Table 3 for statistics details**). This shift was exacerbated in females (p value=0.006) as compared to the males (p value=0.015), although the bacterial communities were similar in the two sexes prior to *Cbx3* inactivation(**Figure 1g)**. The bacterial composition also remained unchanged in *Cbx3* fl/fl female mice treated with tamoxifen in the absence of the Cre recombinase, ruling out an effect solely induced by tamoxifen administration (**Extended data Figure 2**).

As gender may influence IBD risk factors[14], we pursued separate analysis of male and female mice. In female mice, 110 OTUs were modulated in response to HP1 inactivation while in males, only 60 OTU covaried significantly with HP1 inactivation (**Supplementary data Table 4**). In females particularly, we observed an overrepresentation of colitogenic bacteria such *as E. coli and Alistipes*, and a profound down-regulation of anti-inflammatory bacterial species such as the short-chain fatty acids (SCFAs) producer *Ruminococcaceae* **(Extended data Figures 3),** both phenomena being symptomatic of a dysbiotic microbiota reported in IBD[15]**.**

Thus, UC is associated with a reduced expression of HP1γ in the gut epithelium, while inactivation of the cognate gene in the mouse gut results in features typical of gut homeostasis rupture. We concluded that in the colon epithelium, HP1 exerts protective functions, conveying to anti-inflammation and microbiota homeostasis.

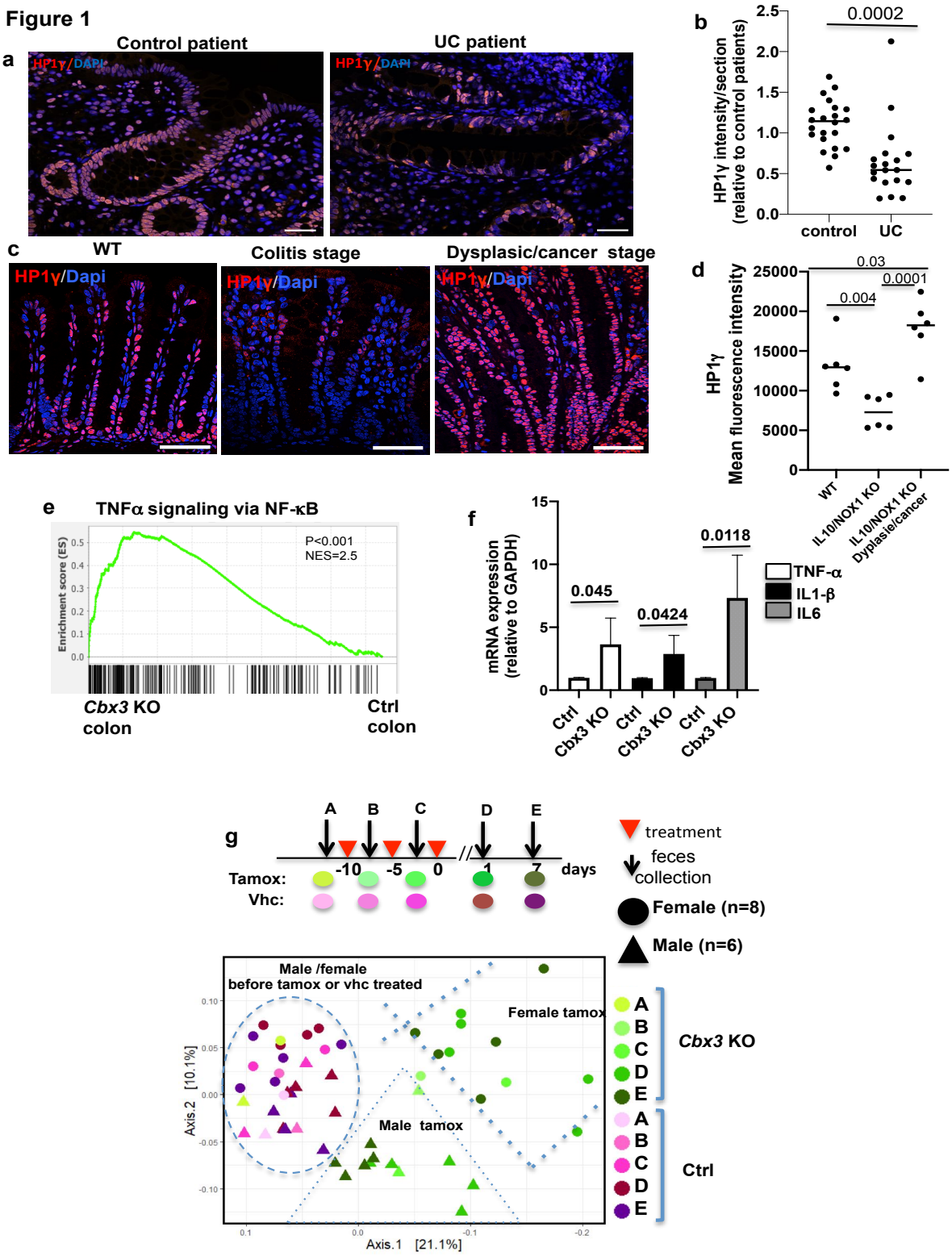

Figure 1: *Cbx3* inactivation in the epithelium leads to gut homeostasis rupture

(a-b) HP1γ expression is affected in UC patients: in (**a**) Representative immunofluorescence in colonic tissue sections stained with anti-HP1γ antibody (red) and Dapi (blue) of colon sections (Scale bar: 50µm) (**b**) ImageJ quantification of the mean fluorescence HP1γ signal intensity/section in control (n=10) and UC patients (n=16), expressed as relative value to control patients (Student's *t* test) (**c-d**) Biphasic expression of HP1γ in the IL10/NOX1 KO mice model: in (**c**) Immunostaining with anti-HP1γ antibody (red) and Dapi (blue) fluorescence, (**d**) ImageJ quantification of the mean florescence Intensity. n=6 mice for each group, Scale bar: 80µm. (Student's *t* test) (**e**) Significant enrichment of the colon *Cbx3* KO transcriptome with pro-inflammatory signature, Two-sided nominal *P* values were calculated by GSEA. (**f**) mRNA expression of TNF-α, IL1-β and IL6 by RT-qPCR from colon epithelium of Ctrl (control) and *Cbx3* KO mice (n=3-4 mice/group, Student's *t* test) (**g**) Temporal evolution of the Beta diversity in Villin-Cre *Cbx3* male and female mice**.** Sheme illustrating the time course of fecal sample collection before (defining group A) and after treatments (Vhc or Tamox) (defining groups B-E), in female (n=8) and male (n=6) mice. Statistical analysis is provided in **Supplementary data Table 3**.

Extended data Figure 1

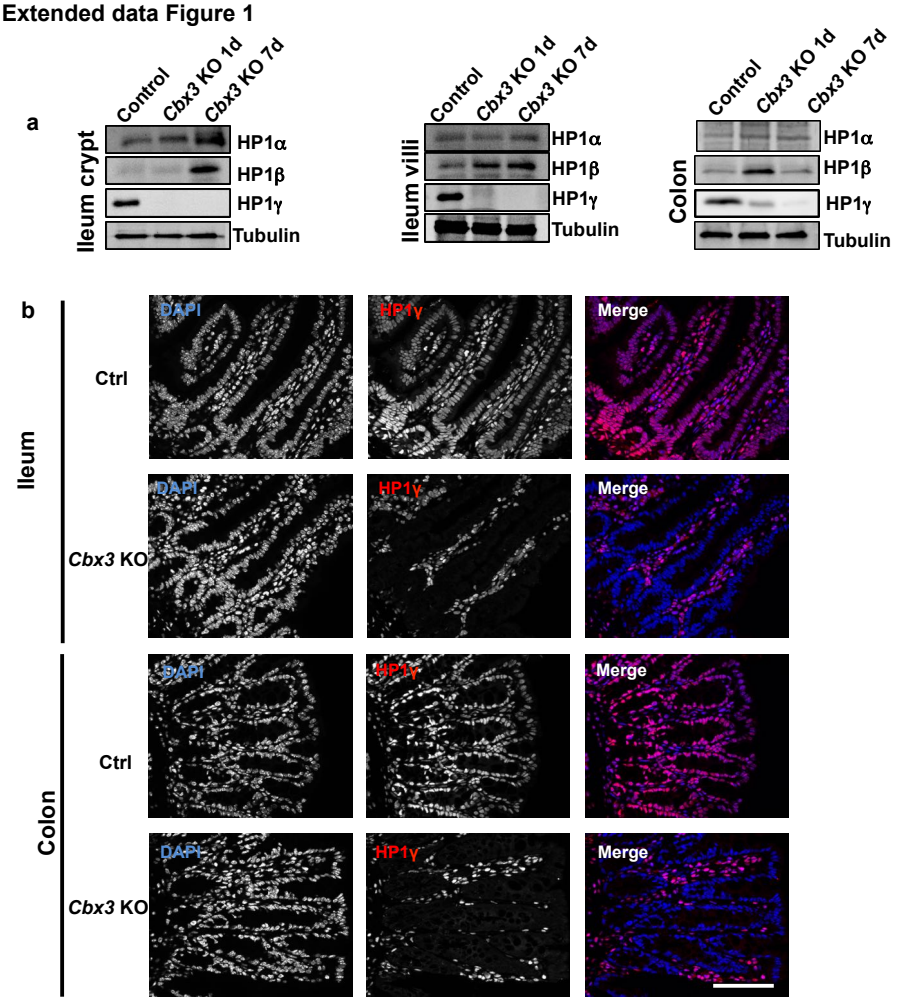

Validation of the *Cbx3* KO mice model (**a**) Western blot analysis: time course of HP1 isoforms expression upon *Cbx3* Knock down 1 day and 7 day post-tamoxifen gavage in the crypt, villi and colon epithelia (**b**) Immunostaining HP1γ in control (Vehicle treated) and *Cbx3* KO mice showing a loss of HP1γ specifically in the epithelium compartment. Scale bar: 80µm.

Extended data Figure 2

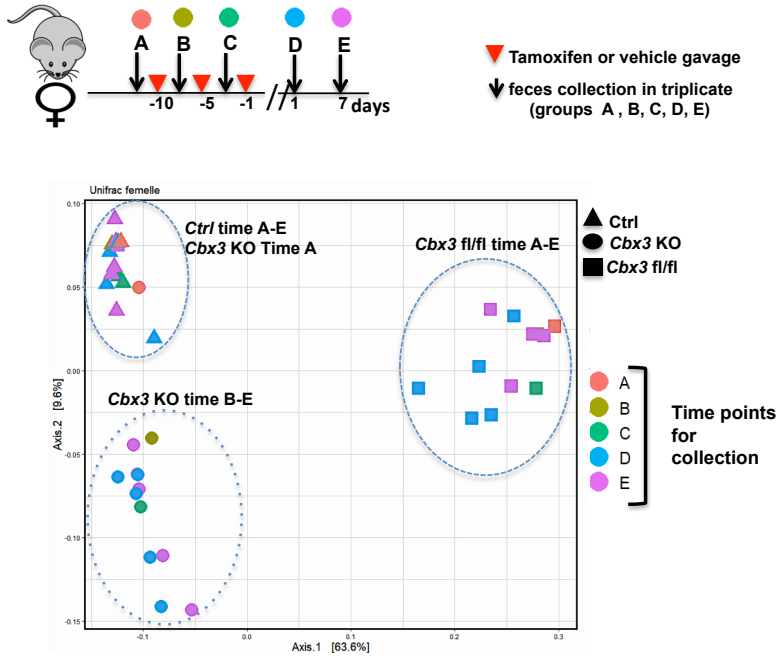

Temporal evolution of the Beta diversity in Villin-Cre *Cbx3* KO female mice before (group A) and after treatments (Vhc or Tamox) (groups B-E): (a) Sheme illustrating the fecal sample collection method before and after treatments in the Ctrl (n=4), *Cbx3* KO (n=4)and *Cbx3* fl/fl (n=3) mice (**b**) Beta diversity showing a shift only in the *Cbx3* KO mice. Tamoxifen treatment did not impact beta diversity in the *Cbx3* fl/fl mice that do not expressed the CRE recombinase.

Extended data Figure 3

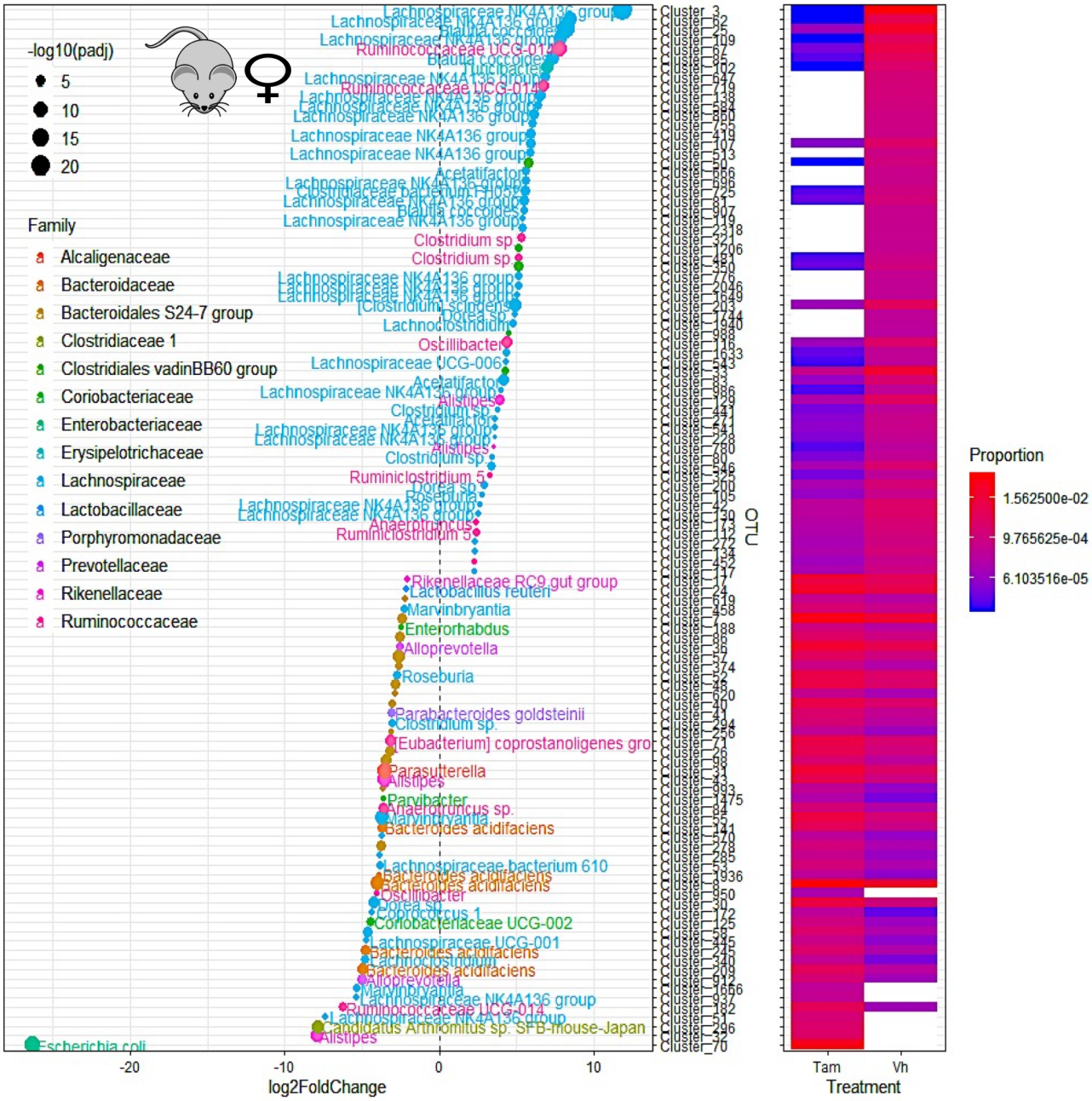

Heat map representing the differentially abundant OTUs between tamoxifen (TAM) and Vehicle (Vh) treated *Cbx3* KO in female mice feces (n=4 in each treated group) with fold change > 2 and significant (P < 0.05). For the graph on the left, each OTU is represented by a dot and colored according to its taxonomic classification at the family level. Taxonomy at the genus or species level is also indicated, when available, next to each OTU. A logarithmic scale (log-2) was used for the x axis

Impact on proliferative homeostasis and maturation

We next delineated the homeostatic functions played by HP1γ in the small intestine. The transcriptome analysis was indicative of a de-silencing of E2F target-genes upon inactivation of *Cbx3* **(Supplementary Data Table 2)**, in agreement with its reported role in retinoblastoma (Rb)-mediated control of cell division[16]. Consistent with an effect of *Cbx3* inactivation on the cell-cycle, the proliferation marker Ki67 in the mutant mice was ectopically detected beyond the normal proliferative compartment, extending all along the crypts and at the base of the villus axes (**Extended data Figure 4a**). Furthermore, a one-hour pulse of the thymine analog 5-bromo-29-

127 deoxyuridine (BrdU), marking cells in S phase, resulted in a frequent labeling of cells
128 at the crypt base containing the intestinal stem cell (ISC) in *Cbx3* KO mice (**Figures**
129 **2a-b)**. In WT mice, this labeling was predominantly confined to the immediate ISC
130 progeny compartment *i.e.* the transit amplifying cells, while for the ISC, BrdU was
131 poorly incorporated, consistent with the prolonged G_1 phase of stem cells[17].
132 Expansion of the stem-cell niche in the *Cbx3* KO mice was also documented by an
133 enlarged area of detection for the Olfm4 marker of stemness (**Extended data**
134 **Figures 4b-c**). Finally, *ex vivo* enteroid 3D matrigel cultures displayed accelerated
135 bud formation when cells were collected from *Cbx3* KO mice (**Extended data**
136 **Figures 5a-b**). However, upon prolonged culture, the bud per organoid ratio
137 drastically dropped in *Cbx3* KO-derived organoids, possibly as a consequence of
138 cellular exhaustion (**Extended data Figures 5a-b**). In the organoids, detection of
139 cells in S-phase by Edu incorporation also revealed aberrantly positive cells along
140 the villus axes, with EdU positive cells filling the lumen of the organoids. (**Figure 2c**
141 **and Extended data Figure 5c**).
142 Along with this altered proliferative homeostasis, villi from mutant mice were subject
143 to maturation defects, as illustrated by a GSEA analysis, showing a strong
144 association between genes deregulated by *Cbx3* inactivation and genes associated
145 with an intestinal stem cell signature, while RT-qPCR reactions revealed increased
146 expression of the stemness markers Ascl2 and Olfm4 in the mutant mice (**Figures 2**
147 **d-e).** Along the villus epithelium of the *Cbx3* KO mice, we also noted expression of
148 nucleolin, a marker of the nucleolus, and electron microcopy studies provided
149 evidence for the presence of nucleoli at the upper part of the villi, with detectable
150 granular components and fibrillar centers **(Figures 2f-g)**. This was in sharp contrast
151 with the expected decline of nucleolin expression along the crypt-villus axis (**Figures**
152 **2f-g**), a consequence of the progressive dilution of ribosomes in the post-mitotic cell
153 populations normally thriving on ribosomes inherited from the progenitor cells[18].
154 Ectopic production of nucleolar organelles was finally documented by an increased
155 18s rRNA production observed at both crypts and villi, in association with an
156 enrichment in genes involved in ribosomal biogenesis **(Figures 2h and Extended**
157 **data Figure 4d).** Thus, the homeostatic repression of nucleolar organelle occurring
158 during epithelial cell maturation was lost. Finally, the production of mature lineages in
159 the *Cbx3* KO mice was affected on both absorptive and secretory lineages. Likewise,
160 GSEA analysis of the RNA-seq data from both compartments showed alterations in
161 the Paneth and enterocyte genes expression programs (**Extended data Figures 4e-**
162 **f**), and we noted a marked defect in the expression of lysozyme, a Paneth cell
163 marker, and of Sucrase Isomaltase, an absorptive enterocyte differentiation marker
164 (**Figures 2i-k**). Overall, these data are indicative of an extensive deregulation in the
165 control of cell proliferation and in the production of mature lineages upon loss *Cbx3*
166 activity.

Figure 2

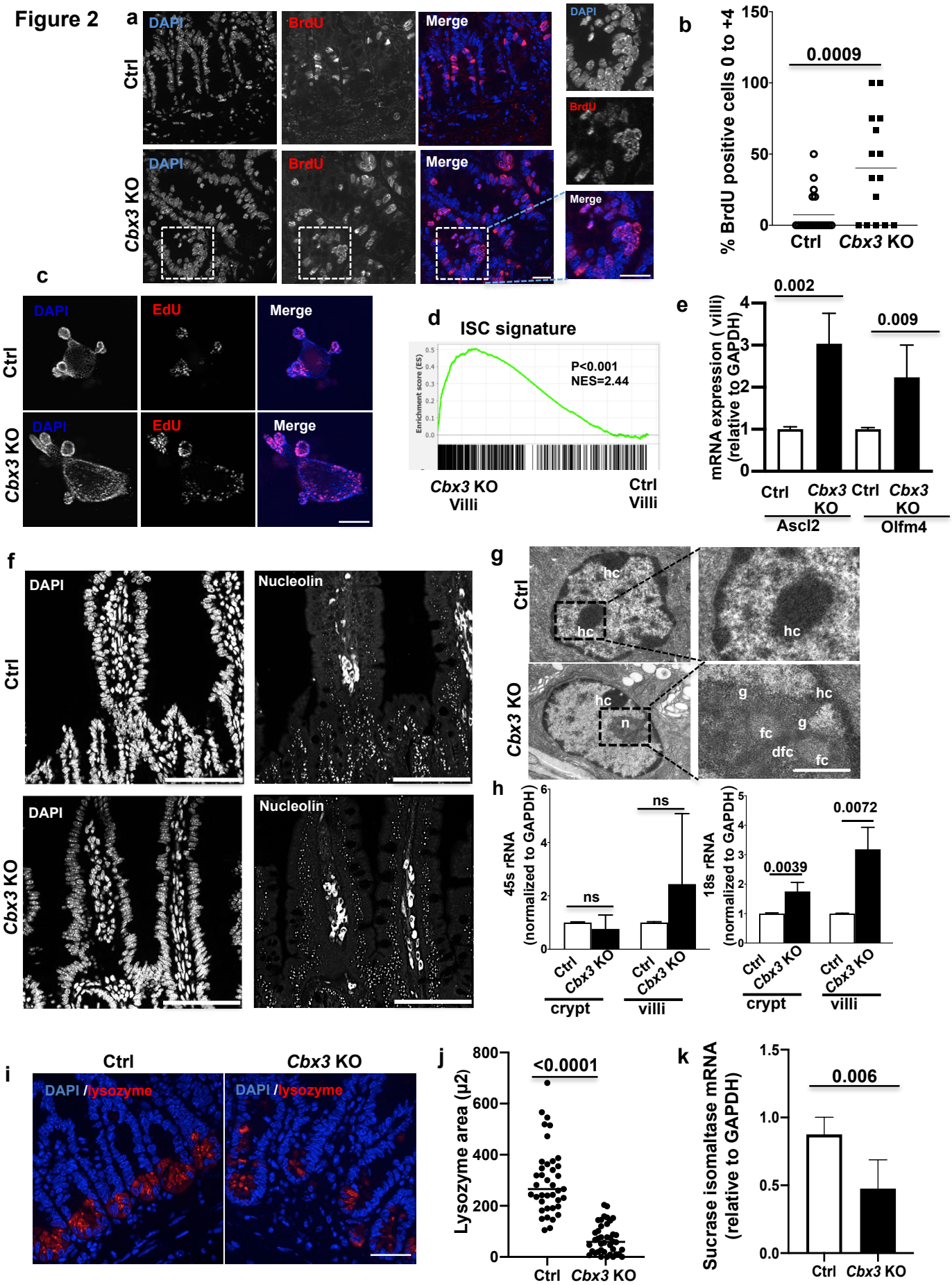
a
DAPI
BrdU
Merge
Ctrl
Cbx3 KO
b
% BrdU positive cells 0 to +4
0.0009
Ctrl
Cbx3 KO
c
DAPI
EdU
Merge
Ctrl
Cbx3 KO
d
ISC signature
P<0.001
NES=2.44
Cbx3 KO Villi
Ctrl Villi
e
mRNA expression (villi) (relative to GAPDH)
0.002
0.009
Ctrl
Cbx3 KO
Ctrl
Cbx3 KO
Ascl2
Olfm4
f
DAPI
Nucleolin
Ctrl
Cbx3 KO
g
hc
n
g
fc
dfc
h
45s rRNA (normalized to GAPDH)
18s rRNA (normalized to GAPDH)
ns
ns
0.0039
0.0072
Ctrl
Cbx3 KO
crypt
villi
i
Ctrl
Cbx3 KO
DAPI /lysozyme
j
Lysozyme area (µ2)
<0.0001
Ctrl
Cbx3 KO
k
Sucrase isomaltase mRNA (relative to GAPDH)
0.006
Ctrl
Cbx3 KO

Figure 2: HP1γ controls epithelial proliferation and maturation in the small intestine

(a) Immunostaining with anti-BrdU antibody (red) and Dapi (blue) of crypt ileal sections from Ctrl and *Cbx3* KO mice (Scale bar: 20µm) (**b**) Quantification of the BrDU positive cells (red) versus Dapi (blue) at the stem cell compartment (0 to +4 position) n=3 animals Ctrl, n=20 sections; *Cbx3* KO n=15 sections; Student's *t* test) (**c**) co-staining EdU (red)/Dapi (blue) in organoids derived from Ctrl and *Cbx3* KO mice (Scale bar: 100µm) (**d**) Significant enrichment of the villi *Cbx3* KO transcriptome with the Lgr5+ intestinal stem cell signature (Munoz et al, 2012), Two-sided nominal *P* values were calculated by GSEA. (**e**) mRNA expression of the stemness markers Olfm4 and Ascl2 by RT-qPCR from villi epithelium of Ctrl and *Cbx3* KO mice (n=3-4 mice/group, Student's *t* test) **(f)** Representative immunofluorescence with nucleolin antibody, n=6 mice/group (Scale bar: 150µm) (**g**) Transmission electron microscopy (TEM) characterizing the nucleolar structure at the upper part of the villi. **g-Left:** Heterochromatin (hc) was observed in the nucleus of ctrl mice. In *Cbx3* KO mice canonical nucleoli (n) were detected, scale bar = 5µm **g-right**: Magnification showing the area of interest with a canonical nucleolus in the *Cbx3* KO mouse (g: granular component; fc: fibrillar centre; dfc; dense fibrillar component). scale bar = 2µm (**h**) rRNA 45S and 18S expression levels in both crypt and villi in the *Cbx3* KO mice (n=3-4mice/group, Student's *t* test) **(i)** Representative immunofluorescence with anti-lysozyme antibody (red) and Dapi (blue) at the ileal crypt (Scale bar: 20µm) (**j**) Quantification of the lysozyme expression area. (n=6 mice/group, with a total of n=40 field /conditions, Student's *t* test) (**k**) mRNA expression of sucrase isomaltase in the villi epithelium (n=4-8 mice, Student's *t* test)

Extended data Figure 4

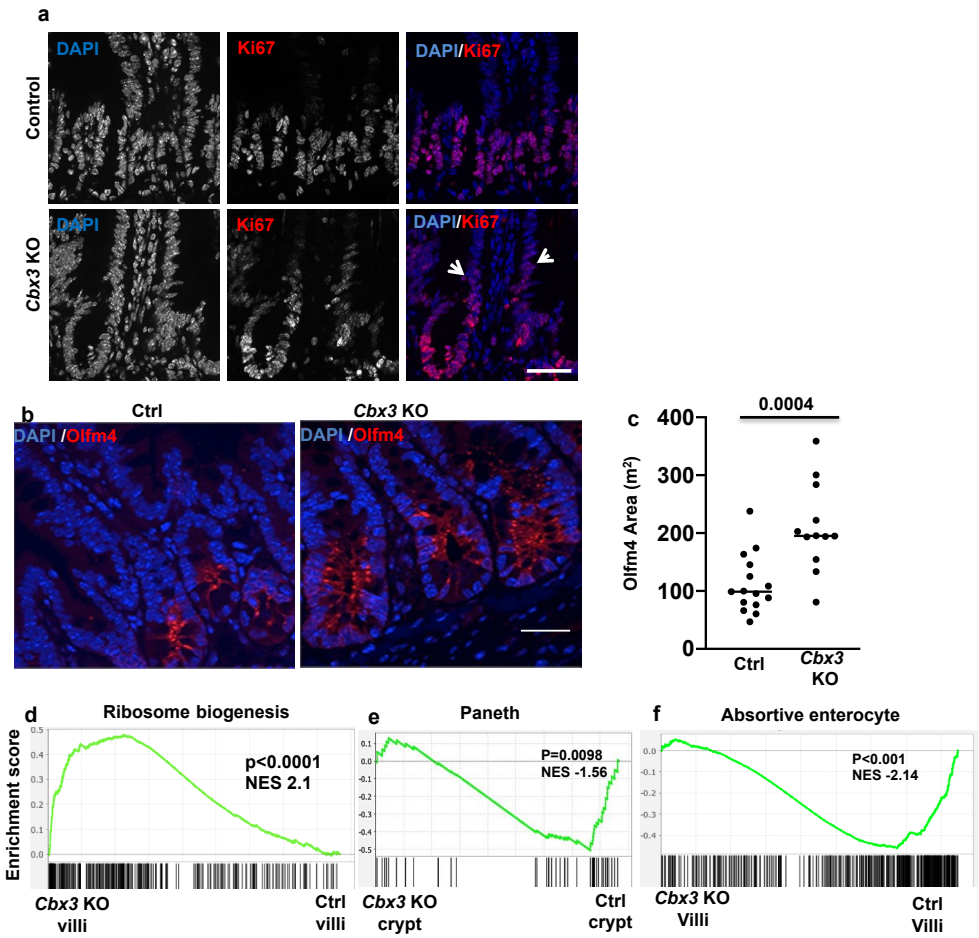

In (a) Extended KI67 signal at the crypt villi axis in the Cbx3 KO small intestine: Representative immunostaining of KI67 (red) and Dapi (blue) in control and *Cbx3* KO mice. Arrow head showed aberrant KI67 signal detected at the base of the villi epithelium. Scale bar: 50µm.
In (b-c) Area of detection of the stem cell mark Olfm4 (**b**) Immunofluorescence with olfm4 antibody (red) and Dapi (blue) of ileal crypt sections from Ctrl and *Cbx3* KO mice, (Scale bar: 50µm) (**c**) Quantification of the Olfm4 expression area. Statistical analysis carried out in n=6 mice, measuring a minimum of 20 fields/mice, Student's *t* test
In (d-f) GSEA analyses: Significant enrichment of the villi *Cbx3* KO transcriptome with ribosomal biogenesis signature (GOBP_RIBOSOME_BIOGENESIS) In **(e-f)** Inverse correlation between *Cbx3* KO and ctrl (control) mice for Paneth and absortive enterocyte signatures (Haber et al, 2017) at the crypt and villi compartments, respectively. Two-sided nominal *P* values were calculated by GSEA.

Extended data Figure 5

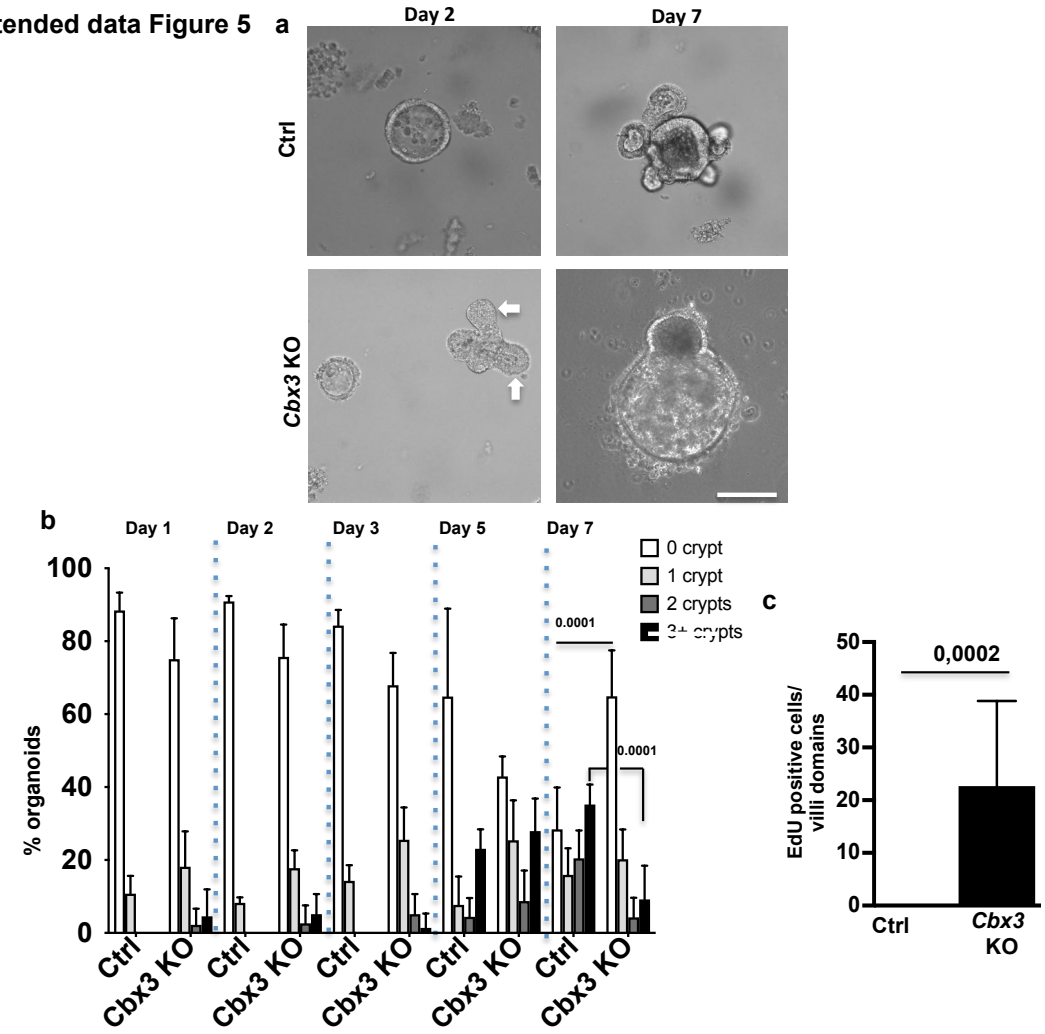

***Ex vivo* enteroid 3D matrigel cultures upon *Cbx3* inactivation: in (a-b)** Time course of organoid budding, (**a**) Representative image, taken by transillumination microscopy. Initial increase in budding formation (white arrows) was not maintained overtime. Scale bar: 80µm. (**b**) Evolution of the number of crypts per organoid over time. At day 7, organoid complexicity (i.e. budding crypt potential) was significantly higher in ctrl, as compared to *Cbx3* KO organoids. Counting was carried out on a minimum of 100 organoids, in three different animals, per condition. Statistical analysis carried out by one-way ANOVA.

In (c) Quantification of the EdU signal in organoids derived from 3 different animals /group, from a total of n=10 organoids/group, Student's *t* test

185 **HP1γ limits usage of poor splice sites**
186 We next sought to define functions for HP1γ on RNA homeostasis in the gut
187 epithelium. Mass spectrometry revealed that HP1γ interactants were highly enriched
188 in component of the spliceosome (**Extended data Figure 6a-c and Supplementary**
189 **Data Table 5**). Among them, we identified members of the catalytic step 2
190 spliceosome (also called U2-type spliceosomal complex C) and splicing factors
191 essential in splice-site recognition, such as the Ser/Arg-rich (SR) proteins family
192 (**Extended data Figure 6c**).
193 This was consistent with earlier reports on the role of HP1γ in the regulation of pre-
194 mRNA splicing[5,19]. Likewise, analysis of the RNA-seq data with the Multivariate
195 Analysis of Transcript Splicing (rMATS) pipeline confirmed that splicing was
196 extensively impacted upon HP1γ inactivation. Significant variations in splicing
197 included a trend towards increase intron retention in the small intestine but not in the
198 colon, with increased and decreased inclusion of alternative exons were observed
199 (**Figure 3a and Supplementary data Tables 6-8,** significant (FDR<0.05) alternative
200 splicing events in crypt, villi and colon epithelia**)**. The absence of a defined pattern in
201 the impact of HP1γ on splicing prompted us to examine whether these numerous
202 splicing events would result from noisy splicing[20], as related in cancer and
203 neurodegeneration [21-24]
204 To that end, we identified unannotated splice junctions present in only one of the two
205 experimental conditions (either WT and Cbx3 KO) for each tissue. Abundance of
206 these junctions that we henceforth will refer to as "*de novo* was significantly
207 increased upon *Cbx3* inactivation (**Figure 3b**). This increase was in a range similar to
208 that observed in cerebellar Purkinje neurons depleted of *Rbm17*, an RNA binding
209 protein reported to repress cryptic splicing usage[23] (**Figure 3b**).
210 Evaluating the quality of the consensus splicing donors and acceptors with a
211 dedicated software revealed that, in average, the *de novo* junctions scored lower that
212 annotated junctions, but higher than random sequences (**Figure 3c)**. This suggested
213 that inactivation of HP1γ promoted usage of poor consensus splice sites, and
214 possibly increased the opportunity range of splicing.
215 Finally, examining splicing noise induced by *Cbx3* inactivation on a gene-per-
216 gene basis further documented that, at a large majority of genes not affected at their
217 expression level, the number of active splice sites was significantly increased (**Figure**
218 **3d and Supplementary data Table 9 for the list of genes)**. These genes included
219 regulators of gut homeostasis. In particular, we noted that the *Pkm* gene, producing
220 both Pkm1 and Pkm2 mRNAs by alternative splicing, the latter safeguarding against
221 colitis[25], showed an extensive increase in *de novo* splicing in the colon (**Figures 3e**
222 **and f, left panels**). Likewise, the *Cdh1* gene encoding E-cadherin product, essential
223 for the epithelial barrier function, and subject to premature termination by alternative
224 splicing[26] was affected by *Cbx3* inactivation at both crypts and colon (**Figures 3e**
225 **and f, middle panels**). Finally, we observed a particularly strong impact at the *Lmna*
226 gene with an average 9-fold increase in *de novo* junctions at the villi (**Figures 3e and**
227 **f, right panel**).

Figure 3

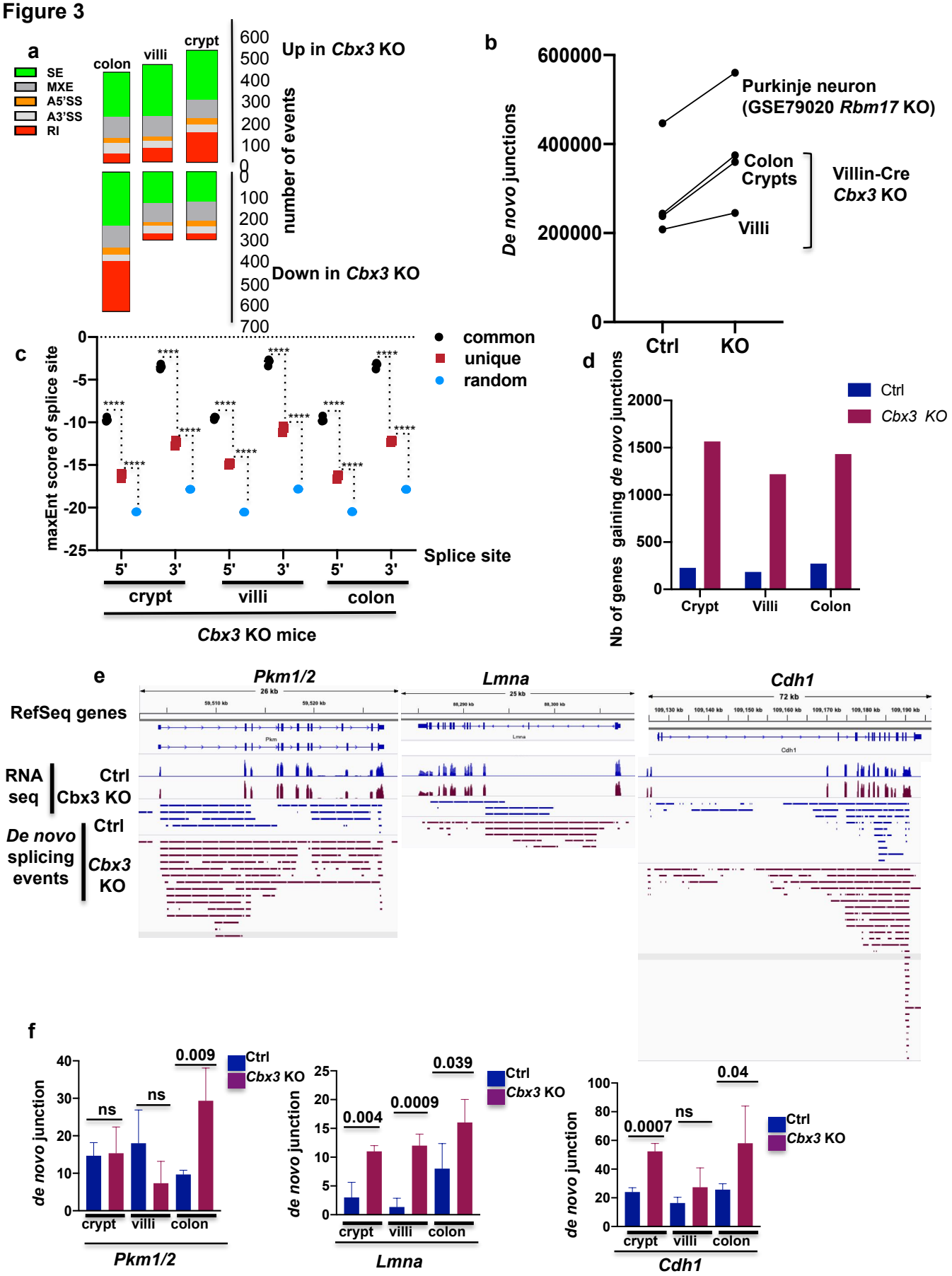
a
SE
MXE
A5'SS
A3'SS
RI
colon
villi
crypt
Up in Cbx3 KO
Down in Cbx3 KO
number of events
b
De novo junctions
Purkinje neuron
(GSE79020 Rbm17 KO)
Colon
Crypts
Villi
Villin-Cre
Cbx3 KO
Ctrl
KO
c
maxEnt score of splice site
common
unique
random
Splice site
5'
3'
crypt
villi
colon
Cbx3 KO mice
d
Nb of genes gaining de novo junctions
Ctrl
Cbx3 KO
Crypt
Villi
Colon
e
Pkm1/2
Lmna
Cdh1
RefSeq genes
RNA seq
Ctrl
Cbx3 KO
De novo splicing events
Ctrl
Cbx3 KO
f
de novo junction
ns
0.009
0.004
0.0009
0.039
0.0007
0.04
Ctrl
Cbx3 KO
crypt
villi
colon
Pkm1/2
Lmna
Cdh1

Figure 3 Impact of HP1γ deficiency on RNA splicing *in vivo*

(a) Types and quantity of splicing alterations detected in the colon, villus, and crypt epithelia. Types of splicing alterations are color coded as indicated. **SE**: skipped exons, **MXE**: mutually exclusive exons, **A3'SS** and **A5'SS**: alternative 3'/5' splice sites, **RI**: retained introns. (**b**) Quantification of *de novo* junctions in control (Ctrl) and *Cbx3* KO (KO) conditions in crypt, villi and colon epithelia after consolidating the 3 RNA-seq replicates from either ctrl or *Cbx3* KO mice in each tissue. *De novo* junctions were defined as junctions not annotated in the mm9 version of the mouse genome and not present in both WT and mutant samples. P-Value was calculated with a paired t-test, n=3. Quantification of *de novo* junctions in *Rbm17* KO mice in Purkinje neurons (GSE79020) is shown (**c**) Consolidated maxEnt score of the *de novo* sites identified with the approach described in (**b**) (red), compared to the score obtained with annotated junctions and that obtained with randomly selected sequences (black and blue, respectively). Values shown are from *Cbx3* KO crypt, villi, and colon (n=3 mice, Ordinary one-way Anova ****p<0.0001). (**d**) *De novo* junctions were quantified at genes that, transcriptionally, were affected less than 2-fold by *Cbx3* KO inactivation. For each indicated condition, we counted genes gaining *de novo* junction 2-fold or more (p Val<0.05). (**e**) *De novo* junctions in colon (PKM and CDH1) or villi (LMNA) were visualized with a genome browser in the neighborhood of the indicated genes. Bars represent the chromosome region located between the 3' and the 5' splice sites for each *de novo* junction. (**f**) Bar graphs show the number of *de novo* junction detected at the corresponding genes at crypt, villi and colon ((n=3 mice for each condition, Student's *t* test).

Extended data Figure 6

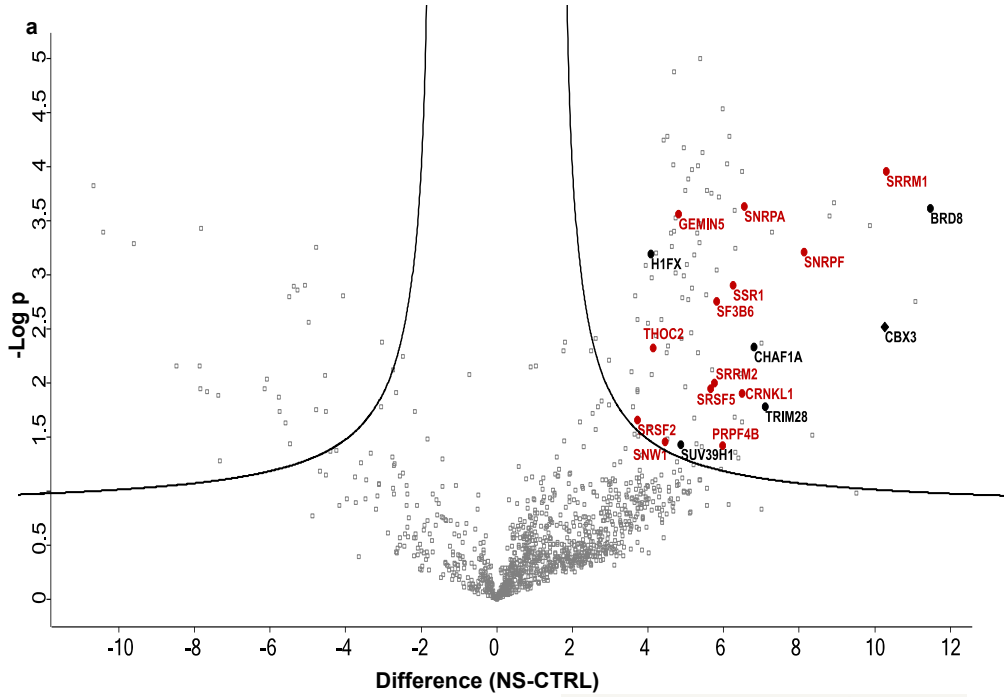

b

Name	P-value	Adjusted p-value
Spliceosome	4.808e-8	0.000004952
Sulfur relay system	0.03815	0.3573
Sulfur metabolism	0.04747	0.3963
RNA transport	0.002130	0.07364

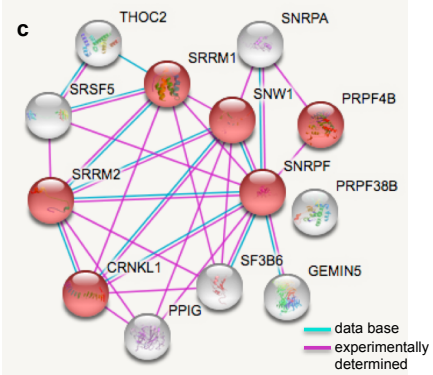

Proteomic analysis: (a) Volcano plot representation of proteins immunoprecipitated with anti-HP1γ or IgG (CTRL) antibodies in HeLa cells and identified by mass spectrometry in 3 independent experiments. X-axis reports the difference of the average of the logarithm of Label Free Quantification (LQF) intensities between IgG control and with anti-HP1γ immunoprecipitates. Y-axis reports the negative logarithm of t-test p value. In black: classical HP1 interactants In red: spliceosome interactants. (**b**) KEGG-pathway analysis on the molecular interactants identified by mass spectrometry (a total of 96 hits). (**c**) Predicted interactions in mass-spectrometry hits matching the KEGG-pathway "spliceosome". Modules in red map to Catalytic step 2 spliceosome (GO:0071013, FDR 4.61e-08).

228 **Control of the progerin splice variant by HP1γ**
229 The biological significance of splicing noise has been poorly characterized in
230 mammals, prompting us to investigate whether the increased usage of *de novo*
231 splice-junctions at the *Lmna* gene in villi lacking HP1γ could result in the production
232 of progerin. Progerin is a splice variant of the Lmna pre-mRNA responsible for the
233 Hutchinson Gilford Progeria Syndrome (HGPS)[27-28]. In this syndrome of premature
234 ageing, production of this splice variant is facilitated by a genomic mutation
235 increasing usage of a progerin splice site that in normal cells is used at low yield
236 upon usage of a poor-consensus splice site[29].
237 We thus applied a taqman assay to the detection of laminA and progerin splice
238 isoforms in the mouse gut epithelium **(Figures 4a-b)**. *Cbx3* inactivation resulted in a
239 significantly increased occurrence of the progerin-specific splicing event in the villus
240 epithelium **(Figure 4b)**. Comparison with colon intestinal epithelium from the *Lmna*
241 G609G HGPS mice revealed that progerin-specific splicing events induced by *Cbx3*
242 inactivation remained less frequent than in cells carrying the *Lmna* G609G mutation,
243 in coherence with the increased strength of the progerin 5'SS provided by the
244 mutation[29](**Figures 4b**). Moreover, sequencing of the PCR end-products confirmed
245 that the splice events detected in *Cbx3* KO mice were identical to the splicing event
246 generated by the HGPS mutation (**Figure 4c**). Levels of the canonical Lamin A
247 splicing events were also increased in both crypts and villi in the mutant mice (**Figure**
248 **4a**), while expression of the *Lmna* gene remained unaltered as documented by the
249 transcriptome analysis (**Figure 3e, middle panel**). Finally, the detection of progerin
250 transcript in the small intestine of the *Cbx3* KO mice was correlated with the
251 production of progerin protein at both villi and crypt epithelia, as visualized by
252 western (**Figures 4d**). In these assays, we used a well-characterized anti-progerin
253 monoclonal antibody, readily detecting the progerin protein in the colon epithelium of
254 HGPS mice (**Extended data Figure 7)**. Of note, the absence of progerin signal in
255 *Cbx3* fl/fl not harboring an inducible Cre-recombinase allowed to rule out an effect of
256 the tamoxifen induction on progerin production (**Figure 4d**). Accumulation of progerin
257 protein in crypts and villi was further documented by immunocytochemistry
258 (**Extended data Figure 8).** This approach revealed that progerin was principally
259 detected at the immediate progeny of ISC (above +4 position, **Figures 4e-f**), thus
260 evidencing for a gradient of progerin expression along the crypt-villi axis in *Cbx3* KO
261 mice. *In vitro* crispr/Cas9-mediated *Cbx3* knockout (KO) in enterocytic TC7 cells
262 confirmed the production of progerin transcripts, and accumulation of
263 nucleocytoplasmic progerin protein (**Extended data Figures 9a-b**).
264 Finally, we examined whether levels of progerin produced upon *Cbx3* inactivation
265 were sufficient to induce toxicity to the nuclear lamina. Observation of the small
266 intestine of *Cbx3* KO mice revealed a misshaping of the nuclear envelope in a
267 fraction of the epithelial cell upon laminB1 immunostaining (**Figures 4g-h**)**.** Similar
268 defects were also observed *in vitro* upon crispr/Cas9-mediated *Cbx3* knockout (KO)
269 in the TC7 enterocytic cell line, resulting in deep invaginations of the nuclear
270 membrane detectable by electron microcopy, reflecting a laminopathy phenotype
271 (**Extended data Figures 9c-d)**. Overall, these data showed that HP1γ defect

272 increased the opportunity range of laminA mRNA splice variants, thus leading to the
273 production of progerin in the absence of HGPS mutation in the gut epithelium.
274 Finally, we investigated whether progerin was also produced in colonic tissue from
275 UC patients, that, as shown **Figures 1a-b,** expressed reduced levels of HP1γ. cDNA
276 were extracted from colon biopsies in non-inflamed zones of healthy individuals
277 (n=17), UC patients (n=19), or Crohn's disease (CD) patients (n=16) with colonic
278 involvement **(Supplementary Data Table 10 for detailed description of the**
279 **population)**. Lamin A and progerin mRNA expressions were determined by taqman
280 assays and accurate transcript detections by sequencing of the PCR end-products.
281 In UC patients, levels of progerin-specific splicing events by taqman assays were
282 significantly up-regulated (p Val= 0.0002), (**Figures 4j-k**), while production of the
283 laminA splicing product was not (**Figure 4i**). No correlation was detected with
284 between progerin mRNA expression and patient age (**Extended data Figure 10a).**
285 Inversely, in CD patients, progerin-specific splicing was unaffected (**Figure 4j**), while
286 the lamin A-specific splicing product was up-regulated (p Val=0.016) (**Figure 4i**), this
287 increase mainly concerning the younger CD patients less than 45 years old, as
288 shown by linear regression analysis **(Extended data Figures 10b-c)**. Thus, progerin
289 transcript emerges as a potentiel marker of UC, while our observations also
290 emphasize the predictive value of the *Cbx3* KO mouse model in this disease.

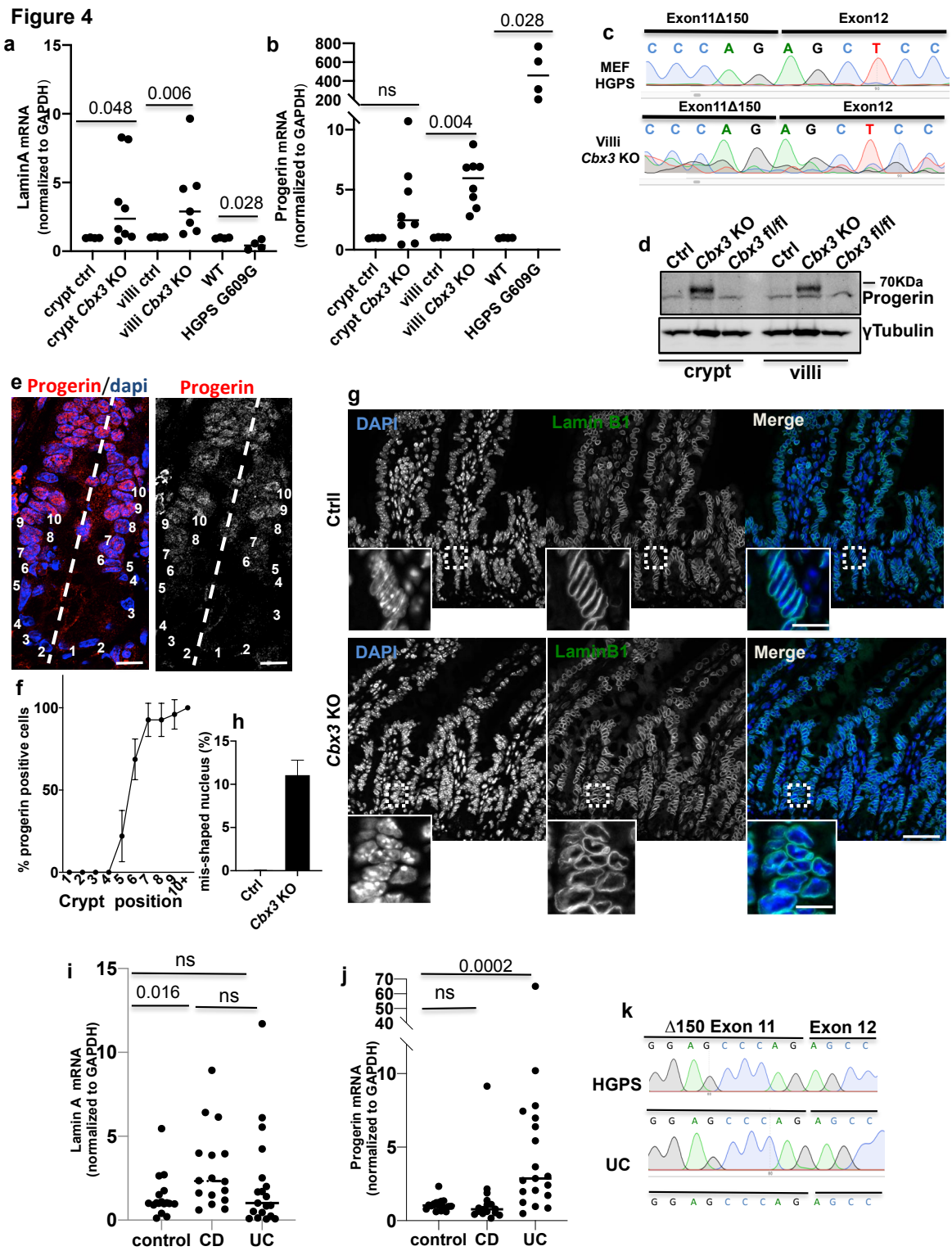

Figure 4: Analysis of progerin production in the gut epithelium

(**a,b**) Taqman Assays laminA and progerin in ctrl (n=4), *Cbx3* KO (n=8), WT and HGPS G609G (n=4mice/group), Mann-Witney U test (**c**) examples of sequencing data of the Taqman PCR end products in villi *Cbx3* KO samples, mouse embryonic fibroblast (MEF) derived from G609G mice used as control (**d**) Immunoblot with anti-progerin monoclonal antibody in epithelium lysates derived from Ctrl, *Cbx3* KO mice and as internal control, *Cbx3 fl/fl* not expressing the Cre recombinase treated with tamoxifen, (**e-f**) Immunofluorescence with anti-progerin antibody (red) and Dapi (blue) and percentage (%) of progerin expressing cells according to the position along the ileal crypt axis (*Cbx3* KO n=23 sections, n=3 mice). Values are represented by the mean with SD. Scale bar: 20µm (**g**) Immunofluorescence with anti-Lamin B1 antibody (green) marking the nuclear envelope (Scale bar: 50µm, Insert: 15µm (**h**) Percentage of cells with misshaping nucleus. n=5 mice in each group, counting in ctrl=4757 nucleus

and *Cbx3* KO=29753 nucleus counted, respectively). Student's *t* test (**i,j**) Taqman Assays laminA and progerin in control (n=17), Crohn disease (CD, n=16) and Ulcerative colitis (UC,n=19) populations, cDNA were extracted from colon biopsies. Mann-Witney U test (**k**) example of sequencing data from the Taqman PCR end products in one UC patient, Human fibroblast from HGPS patient was used as positive control, UC= Ulcerative colitis.

Extended data Figure 7

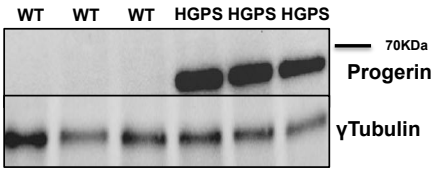

Progerin expression detected by Immunoblot in colon epithelium lysates derived from 12 months old WT and heterozygote HGPS G609G mice (n=3 mice in each group)

Extended data Figure 8

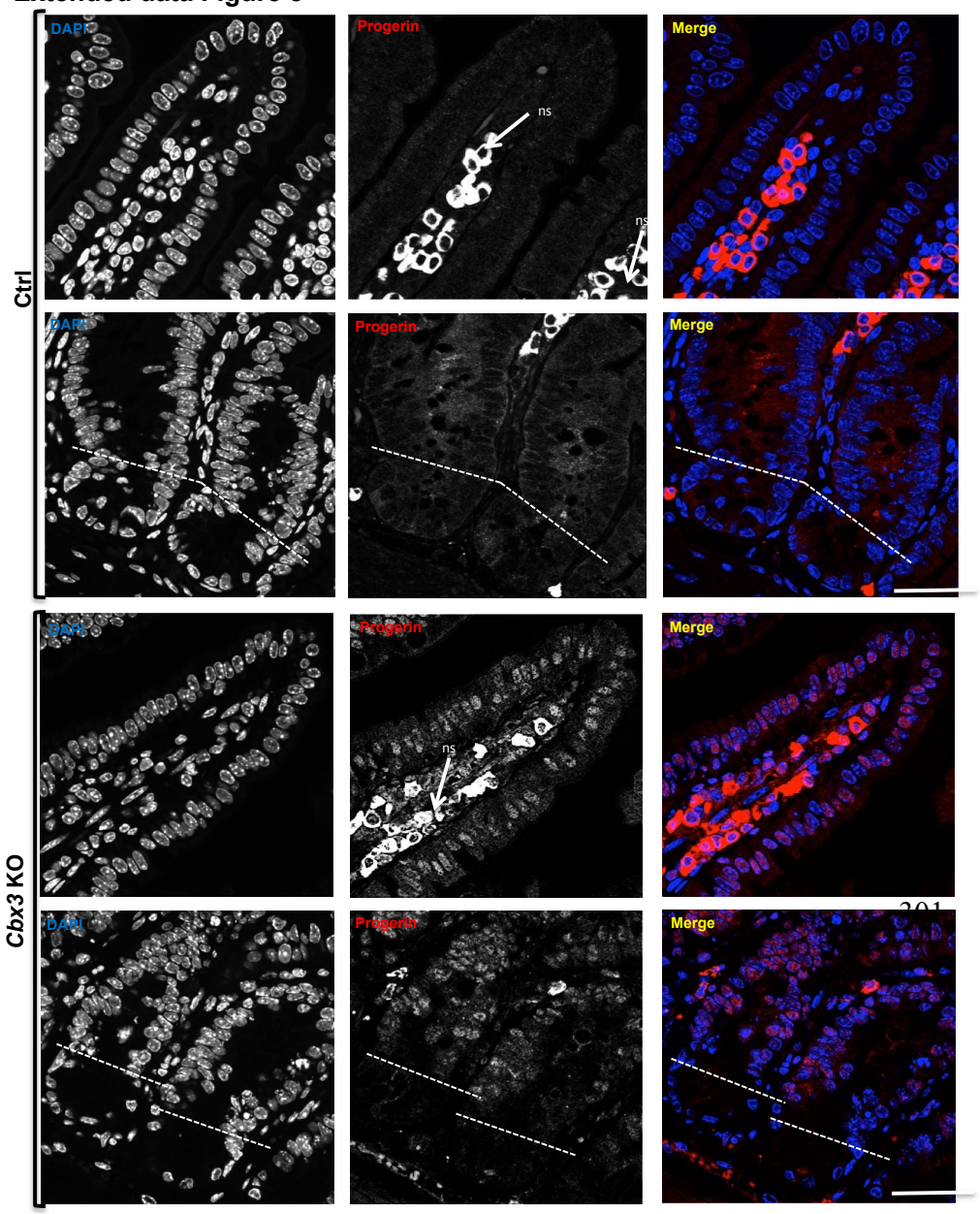

Representative immunostaining of progerin in the ileon crypt and villi epithelia: progerin signal (red) is detected in the nucleus (Dapi, blue) *ns= non specific labeling (detectable with secondary antibody alone), dashed line showing the stem cell compartment at the intestinal crypt (position O to +4) (Scale bar: 80µm)

Extended data Figure 9

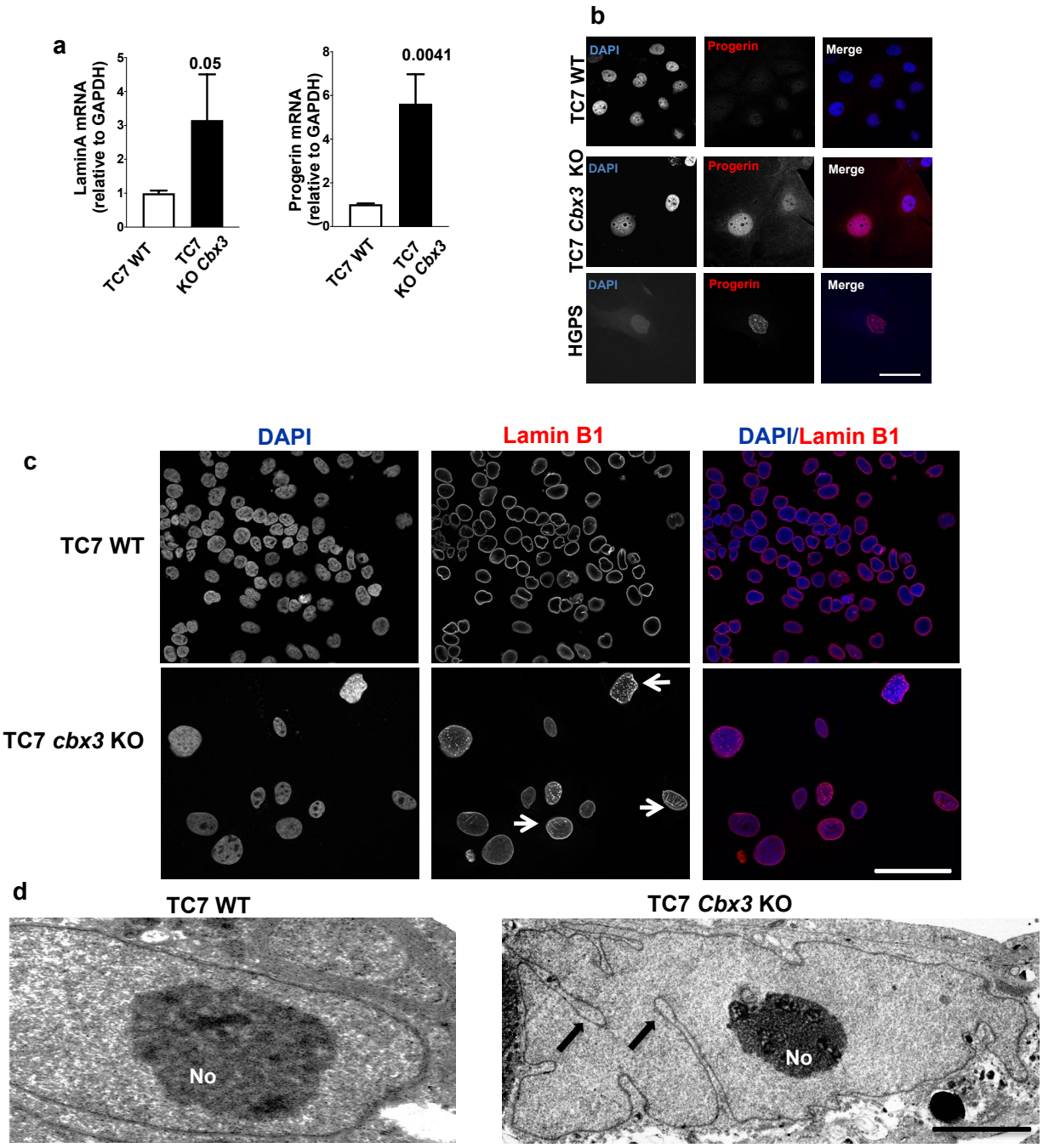

***Cbx3* inactivation leads to a laminopathy with progerin production in the Crispr/Cas9 *Cbx3* enterocytic cell line TC7 (TC7 *Cbx3* KO)**. (**a**) RT-qPCR lamin A and progerin in the WT and Crispr/Cas9 *Cbx3* enterocytic cell line TC7 (TC7 *Cbx3* KO). Values are represented by the mean with SD of 3 independent experiments, Student's *t* test (**b**) Representative immunofluorescence with anti-progerin antibody (red) and Dapi (blue) in WT, TC7 *Cbx3* KO and human HGPS fibroblast **(c)** Immunostaining with anti-lamin B1 antibody: laminB1 signal (red) reveals mis-shaping at the nuclear envelop (white arrow) reminiscent of progeria cells (Scale bar: 50µm).(**d**) Transmission Electron Microscopy (TEM) on TC7 cells (WT and *Cbx3* KO). The nuclear envelop shows multiple invaginations in TC7 *Cbx3* KO cells (black arrows). No = Nucleolus. (Scale bar: 2µm WT, 5µm *Cbx3* KO)

Extended data Figure 10

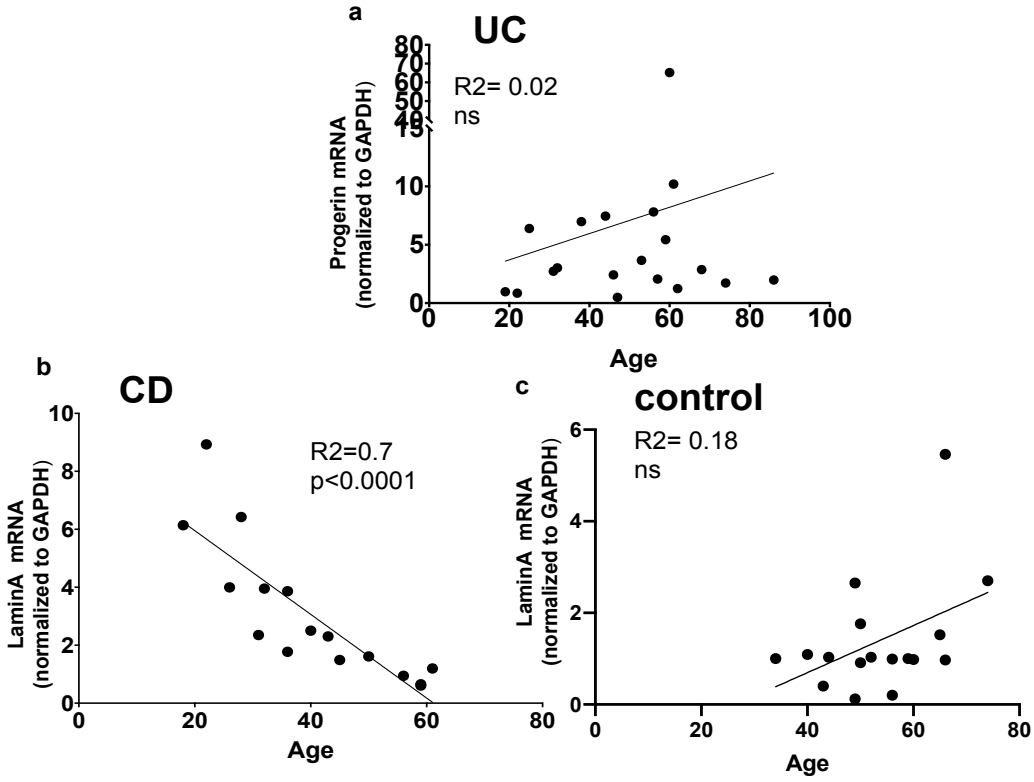

In (**a**) Simple regression analyses for progerin mRNA expression in UC (ulcerative colitis) patients relative to the age
In (**b-c**) Simple regression analyses of laminA mRNA expression relative to the age in (**a**) CD (Crohn's disease) and (**c**) control patients. The pvalue corresponds to the linear regression of laminA expression vs age

Discussion

This work seminally defined HP1γ as a mechanism safeguarding RNA splicing accuracy in the gut epithelium, limiting the impact of naturally occurring non-canonical splicing events. Non-canonical splicing activity is frequently referred to as "splicing noise"[20] . While noisy splicing in non-mammalian animal model may promote diversity in mRNA splice variants, with possible physiological functions[30-31], in mammals, its significance remains elusive, and seen as a pervasive erroneous splicing activity, possibly involved in genome evolution[32]. As a matter of fact, this phenomenon has been linked to human pathology, with global activation of noncanonical splicing sites, as detected in cancer and neurogenerative diseases [22-24,33]. Only few RNA binding proteins, including Rbm17, hnRNP and TP43[23-24], were shown to dampen cryptic splicing genome-wide and our study highlights a fundamental role for HP1 in this process in the gut epithelium. In this context, HP1γ deficiency was sufficient to induce the production of progerin, a normally repressed splice variant. To our knowledge, HP1γ is the first identified *in vivo* mechanism regulating progerin production in the absence of the HGPS mutation. The effects of HP1γ inactivation on splicing was accounted for by an apparently general reduction in

319 the precision of splicing. Specifically, junction reads were increasingly detected at
320 non-annotated splice junctions, and at sites with very poor donor or acceptor
321 consensus sequences. While our understanding of this decreased stringency in
322 splice site selection is still incomplete, we note that our proteomic approach to
323 HP1γ molecular partners detected numerous splicing factors ensuring the usage of
324 only genuine splice sites. These included components of the major (U2-dependant)
325 spliceosome as well as auxiliary splicing factors essential for spliceosome recognition
326 of the consensus sequence. Among these, the Ser/Arg-rich (SR) proteins, were
327 previously shown to modulate usage of the splice sites implicated in the production of
328 progerin in the absence of the HGPS mutation, possibly by interfering with exonic
329 splicing enhancers (ESE) involved in proper exon recognition by SR proteins[34,29]. We
330 thus propose a model in which the chromatin-associated HP1γ participate in the
331 precise co-transcriptional recruitment of regulators of pre-mRNA splicing. The
332 reliance of HP1γ on auxiliary regulators of splicing may also be illustrated by its
333 regional impact on splicing, possibly as a function of the splicing regulators available
334 in each tissue or cell type. In particular, we noted a gradient of progerin expression
335 along the crypt-villi axis, leaving out the ISC compartment. The latter suggests a
336 modulation of splicing possibly linked to the cellular developmental state, a notion
337 further supported by the HGPS-iPSCs model, in which progerin was only observed
338 upon cell commitment[35]. While our data mainly points toward an impact of HP1γ via
339 spliceosome recruitment, an involvement for HP1γ in the degradation of defective
340 splicing products may also be considered, as suggested by the implication of the
341 yeast HP1 homolog in escorting pericentromeric transcripts to the RNA decay
342 machinery[36].
343 Before a role for HP1 was described in splicing, this protein was mainly known as a
344 mediator of heterochromatin-dependent silencing, repressing transcription at
345 repeated DNA sequences, including rDNA loci, and at a subset of gene promoters
346 [8,16,37-40]. This repressive function of HP1γ was found to also have a clear impact on
347 the biology of the small intestine, participating in the regulation of the nucleolar
348 organelles, and in the silencing of genes controlling proliferative homeostasis. These
349 observations illustrate the homeostatic functions of HP1γ involved in essential
350 activities in both heterochromatin and euchromatin. The previously described role of
351 HP1 in tissue longevity across the species[40-41] may be largely rooted in this
352 polyvalence.
353 While no human disease has been clearly linked to HP1 gene mutations, decreased
354 HP1 expression was reported in syndromes of accelerated aging, including the
355 Werner syndrome and HGPS[42-44]. We similarly identified a potent reduction of HP1
356 expression in UC patients as well as in mouse model relevant for this disease. From
357 our *Cbx3* KO mouse model, we concluded that HP1γ deficiency may support
358 aberrant pathways nurturing both inflammation and splicing defects at key
359 homeostatic genes. Likewise, the increased detection of progerin in UC colon tissue
360 prompts us to speculate that, alike what we observed in the *Cbx3* KO mice, the lamin
361 A splice variant is only the “tip of the iceberg”, indicative of a more extensive

362 disturbance in RNA splicing precision endured by UC patients. Still in its infancy with
363 regard to intestine disease[45-47], the identification of mechanisms relying on RNA
364 splicing dysfunctions should transform our understanding of the functional decline in
365 the gut epithelium of IBD patients.

366 **Methods**

367 **Mouse models**

368 *Cbx3*$^{fl/fl}$ mice (provided by Dr Florence Cammas, IRCM, Montpellier, France) were
369 crossed with Villin-CreERT2 mice (provided by Dr Cohen-Tannoudji, Institut Pasteur,
370 Paris, France) to produce the Villin-creERT2:*Cbx3-/-* mouse model (this study).
371 Heterozygote *Lmna*$^{G609G/G609G}$ mice (here referred as HGPS mice) were provided by
372 Dr Maria Eriksson (Karolinska Institutet, Sweden). Mice were fed by a standard diet
373 (SD) rodent chow (2018 Teklad Global 18% Protein Rodent Diet, Harlan) composed
374 of 60% carbohydrate fed *ad libitum*. Tamoxifen (0.5mg/g) diluted in 20% clinOleic
375 acid was administrated by oral gavage, at 3 doses every 5 days as described[48].
376 Control mice received 20% clinOleic acid alone by oral gavage. Additional controls
377 using *Cbx3*$^{fl/fl}$ mice that do not express the Cre recombinase were identically treated
378 with tamoxifen. All the experiments using Villin-creERT2:*Cbx3-/-* mouse model were
379 performed with mice 2-3 months of aged. BrdU (Sigma) was injected intraperitoneally
380 (i.p.) at 100 μ g/g animal body weight, 1h prior to sacrifice.

381 **Patients and Biopsy Specimens**

382 All patients were followed in the Department of Gastroenterology (hôpital Beaujon,
383 Paris). The protocol was approved by the local Ethics Committee (CPP-Ile de France
384 IV No. 2009/17, and No2014-A01545-42) and written informed consent was obtained
385 from all patients before enrollment. Colonic pinch biopsy allowing the extraction of
386 the epithelial layer was obtained during endoscopic investigation in non-inflamed
387 areas to allow a comparison with healthy tissues in the control population. Biopsies
388 were performed in the right or the left colon or in case of cancer at least 10 cm away
389 from the cancer site. For the immuno-histological study, 26 patients were included,
390 with 10 healthy control and 16 UC patients (detailed of the population provided in
391 **Supplementary data Table 1**). For the transcriptional study, 56 patients were
392 included, with 17 healthy controls, 19 UC and 16 CD patients with colonic
393 involvement (detailed of the population provided in **Supplementary data table 10**).
394 Total RNA was extracted from human biopsies with RNAble (Eurobio) and quantified
395 using a ND-1000 NanoDrop spectrophotometer (NanoDrop Technologies). Reverse
396 transcription of total mRNA was performed using M-MLV RT (Invitrogen) according to
397 the manufacturer's recommendations.

398 **Cell cultures**

399 Human dermal fibroblasts patients who carried the HGPS p.Gly608Gly mutation were
400 obtained from the Coriell Cell Repository. Caco2 (TC7 cells) were used to generate
401 the CRISPR/Cas9-mediated *Cbx3* cell line. The pSpCas9(BB)-2A-GFP (PX458)
402 vector expressing Cas9 endonuclease (gift from Feng Zhang, Addgene plasmid #
403 48138) was linked with a single-guide RNA (sgRNA) designed specifically for *Cbx3*
404 gene. Two Sequence guides (GAAGAAAATTTAGATTGTCC and

405 GAATATTTCCTGAAGTGGAA) were defined by ZiFiT Targeter Version 4.2 software.
406 Insertion of the sequence guide was performed in the BbsI restriction site of the
407 PX458 vector and check by sequencing. Transfection in TC7 cells was performed by
408 lipofectamine 2000 and singles clones for each sequence guide were selected by
409 FAX according to the GFP signal.

410 **Immunofluorescence**

411 Intestine (ileum or colon) was collected and washed with PBS at 4ºC and cut in
412 pieces about 5 mm. Intestinal fragments were fixed with formalin overnight at 4ºC.
413 Once fixed, intestinal fragments were included in paraffin blocks. Paraffin sections
414 were done in a microtome Leica RM2125 RTS, with a thickness of 4μm.
415 Subsequently, the deparaffinization and rehydration of the samples was carried out
416 by immersion in Xylene (2x10 min), absolute ethanol 5 min, 90% ethanol 5 min, 70%
417 ethanol 5 min and distilled water (2x5 min), all at R.T. Finally, the antigen was
418 unmasked using the EDTA boiling technique for 30 min at 95ºC, followed by 20 min
419 at R.T. All samples were sequentially treated with 0.1 M glycine in PBS for 15 min,
420 3% BSA in PBS for 30 min and 0.5% Triton X-100 in PBS for 2h (mouse tissue). In
421 case of nucleolin staining, tissue sections were incubated during one minute at RT
422 with proteinase K 0.05mg/ml, followed by a wash with glycine 2mg/ml during 15
423 minutes at RT. They were then incubated with primary antibodies overnight at 4 °C,
424 washed with 0.05% Tween-20 in PBS, incubated for 1h in the specific secondary
425 antibody conjugated with Alexa 488 or Cy3 (Jackson, USA), 15 min with DAPI
426 (1μg/ml), washed in PBS and mounted with the antifading medium VECTASHIELD®
427 (Vector laboratories). Anti-HP1γ (2MOD-IG6, Thermo Scientific), HP1β (1MOD-1A9,
428 Thermo Scientific), HP1α (2H4E9, Novus Biologicals), KI67 (ab16667, Abcam),
429 Olmf4 (D6Y5A, Cell Signalling), Brdu (MA3-071, Thermo Scientific), laminB1
430 (ab65986, Abcam), Progerin (13A4DA, sc-81611, Santa Cruz), γTubulin (4D11,
431 Thermo Scientific), and Nucleolin (ab22758, Abcam) were used as primary
432 antibodies. Nuclei were stained using 4 ,6-diamidino-2-phenylindole (DAPI, 62248,
433 Thermo Scientific).
434 Microscopy images were obtained with a ZEISS Apotome.2 (Zeiss, Germany),
435 structured illumination microscope, using a 63× oil (1.4 NA) objective. To avoid
436 overlapping signals, images were obtained by sequential excitation at 488 and
437 543 nm in order to detect A488 and Cy3, respectively. Images were processed using
438 ZEISS ZEN lite software. The quantitative analysis of the immunofluorescence signal
439 was performed on ImageJ. The values are represented with Mean fluorescence
440 intensity, relatives to control samples.

441 **Tissue processing for intestinal epithelial cells isolation and organoids culture**

442 The technique was adapted from *Nigro* et al, 2019[49]. Small intestine or colon were
443 collected and washed with PBS at 4ºC and cut in pieces of about 5 mm in length. For
444 epithelial isolation, intestinal fragments were incubated 30 min at 4ºC in 10mM EDTA
445 after which they were transferred to BSA 0,1% in PBS and vortexed 30-60 s. The
446 supernatants (containing the epithelial cells) were filtered with a 70μm cell strainer. At
447 this step, crypts went through the cell strainer and villi were retained on it. Crypt and

448 villus fractions were then centrifuged separately and the pellets were frozen in liquid
449 nitrogen until processed. The quality of the separation was accessed by the
450 expression of selective expression of stemness markers in the crypts but not villi, as
451 confirmed by RNA sequencing. For organoid production, crypt pellet was
452 disaggregated and cultured in Matrigel as described [49]. EdU staining was performed
453 using Click-iT™ EdU Cell Proliferation Kit for Imaging (Thermo fisher), following
454 manufacturer indications.

455 **Transmission electron microscopy**

456 In TC7 cells, Transmission Electron Microscopy (TEM) was performed by
457 cryofixation/freeze substitution method. Cells were fixed overnight at 4ºC with 3.7%
458 paraformaldehyde, 1% glutaraldehyde, in 0.1 M cacodylate buffer. After fixation, cells
459 were pellet and contrasted with osmium tetroxide (OsO_4) and uranyl acetate. Then,
460 cells were included in freeze-substitution medium during at least 3 days at -80ºC,
461 dehydrated in increasing concentrations of methanol at −20 °C, embedded in
462 Lowicryl K4 M at −20 °C and polymerized with ultraviolet irradiation. Ultrathin
463 sections were mounted on nickel grids, stained with lead citrate and uranyl acetate
464 and examined with a JEOL 1011 electron microscope.

465 Intestinal tissue fragments around 500mm were fixed overnight at 4ºC with 3.7%
466 paraformaldehyde, 1% glutaraldehyde in 0.1 M cacodylate buffer overnight at 4º.
467 Small tissue fragments were washed in 0.1 M cacodylate buffer, dehydrated in
468 increasing concentrations of methanol at −20 °C, embedded in Lowicryl K4 M at
469 −20 °C and polymerized with ultraviolet irradiation. Ultrathin sections were mounted.

470 **Real time quantitative PCR analysis**

471 Total RNA was extracted using Trizol (TR-118, Molecular Research Center, Inc.)
472 following the manufacturer's instructions and DNAse treatment. RNA samples were
473 quantified using a spectrophotometer (Nanodrop Technologies ND-1000). First-
474 strand cDNA was synthesized by RT-PCR using a RevertAIT H Minus First Strand
475 cDNA Synthesis kit (Thermo Scientific). qPCR was performed using the Mx3005P
476 system (Stratagene) with automation attachment. For progerin and laminA detection,
477 real-time PCR amplification was carried out with the TaqMan" Gene Expression
478 Master Mix (life technologies) using predesigned primers for mouse GAPDH
479 (Mm99999915_g1), mouse lamin A that do not recognized progerin or DNA (Assay
480 ID : APGZJEM), mouse progerin (F: ACTGCAGCGGCTCGGGG R:
481 GTTCTGGGAGCTCTGGGCT and probe: CGCTGAGTACAACCT), human lamin A
482 (F: TCTTCTGCCTCCAGTGTCACG R: AGTTCTGGGGGCTCTGGGT and probe
483 ACTCGCAGCTACCG), human progerin (F: ACTGCAGCAGCTCGGGG R:
484 TCTGGGGGCTCTGGGCTCCT and probe CGCTGAGTACAACCT), human GAPDH
485 (Hs00266705_g1). For SYBRGreen (Takara) based qPCR, the following primers
486 have been used: mouse Ascl2 (F: GGT GAC TCC TGG TGG ACC TA ; R: TCC GGA
487 AGA TGG AAG ATG TC) mouse Olfm4(F:ATC AGC GCT CCT TCT GTG AT R:
488 AGG GTT CTC TCT GGA TGC TG) mouse TNF-α (F :
489 GATCTCAAAGACAACCAACATGTG R : CTCCAGCTGGAAGACTCCTCCCAG)
490 mouse IL1-β (F :TACAGGCTCCGAGATGAACAAC R :

491 TGCCGTCTTTCATTACACAGGA) mouse IL6 (F : ACTTCCATCCAGTTGCCTTCTT
492 R: CAGGTCTGTTGGGAGTGGTATC) mouse Sucrase isomaltase (F:
493 CGTGCAAATGGTGCCGAATA R: TCCTGGCCA TACCTCTCCAA) GAPDH (F:
494 TGACCACAGTCCATGCCATC; R: GACGGACACATTGGGGGTAG) mouse 45S (F:
495 GAACGGTGGTGTGTCGTT; R: GCGTCTCGTCTCGTCTCACT). Mouse 18S: (F:
496 GATGGTAGTCGCCGTGCC; R: CCAAGGAAGGCAGCAGGC).

497 **RNA sequencing and bioinformatic pipelines**

498 Total RNA was extracted from control and *Cbx3* KO epithelial cells from the small
499 intestine (crypts and villi) and colon epithelia (n=3 for each group of mice, so in total
500 6x3=18 RNA samples) by guanidinium thiocyanate-phenol-chloroform extraction and
501 DNAse treatment, following the manufacturer specifications. Total RNA library
502 preparation and sequencing were performed by Novogene Co., Ltd, as a lncRNA
503 sequencing service, including lncRNA directional library preparation with rRNA
504 depletion (Ribo-Zero Magnetic Kit), quantitation, pooling and PE 150 sequencing
505 (30G raw data) on Illumina HiSeq 2500 platform. Filtering and trimming of the RNA
506 seq data left around 230-300 million reads pairs /sample.
507 Gene expression analysis and differential splicing analysis was carried out by
508 Novogene Co., Ltd, using the DESeq2 (v1.18.1) package[50] and rMATS (v4.1.0)[51]
509 (parameters: --libType fr-firststrand –novelSS), respectively, on the mm10 mouse
510 reference genome. For assessment cryptic splice sites, in house RNA-seq data and
511 publicly available Rbm17 KO RNA-seq data (GEO GSE79020) were realigned on the
512 mouse mm9 annotation file from Ensembl (version 67). The resulting BAM files were
513 used to generate bigwig files, using bamCoverage (parameter: --normalizeUsing
514 CPM) from Deeptools (v3.1.3)[52] Coordinates of annotated and unannotated junctions
515 were then retrieved from the BAM files using regtools
516 (https://github.com/griffithlab/regtools). For each of the 6 conditions, unannotated
517 junctions from the 3 replicates were pooled, before eliminating junctions present both
518 in WT and KO conditions. Finally, junctions spanning over 20kb were filtered away as
519 possible artefacts of the alignment. The remaining junctions, never shared between
520 WT and mutant samples, were considered *de novo*. To quantify the strength of the
521 splice sites, DNA sequences comprising the last 3 nucleotides of the exon and the
522 first 6 nucleotides of the intron were recovered for the 5′ end of the junction. For the 3′
523 end of the junction, the sequences of the last 20 nucleotides of the intron and the first
524 3 nucleotides of the exon were recovered. Then, the splice sites strength was
525 computed for each junction using the MaxEnt algorithm[53]. The MaxEnt algorithm was
526 also applied to randomized junctions generated by applying the “shuffle” function of
527 the bedtools suite (v.2.25.0)[54] to the .bed files containing de novo junctions.
528 GSEA analysis was performed (with -nperm 1000 -permute gene_set -collapse false
529 parameters) using the same expression matrix (v2.2.2), comparing ctrl and *Cbx3* KO
530 samples at the crypt, villi and colon. Transcriptional signatures used for the analysis
531 were extracted from the literature for lgr5 ISC signature[55] , enterocyte and Paneth
532 cell signatures[56] and GSEA data bases (MSigDB hallmark gene set).
533
534

535 **Fecal microbiota analysis by 16S rRNA gene sequencing**
536 Genomic DNA was obtained from fecal samples using the QIAamp power fecal DNA
537 kit (Zymo Research), and DNA quantity was determined using a TECAN Fluorometer
538 (Qubit® dsDNA HS Assay Kit, Molecular Probes). The V3-V4 hypervariable region of
539 the 16S rRNA gene was amplified by PCR using the following primers: a forward 43-
540 nuclotide fusion primer 5′ **CTT TCC CTA CAC GAC GCT CTT CCG ATC T**AC GGR
541 AGG CAG CAG3 consisting of the 28-nt illumina adapter (bold font) and the 14-nt
542 broad range bacterial primer 343F and a reverse 47-nuclotide fusion 5′ **GGA GTT**
543 **CAG ACG TGT GCT CTT CCG ATC T**TA CCA GGG TAT CTA ATC CT3′
544 consisting of the 28-nt illumina adapter (bold font) and the 19-nt broad range
545 bacterial primer 784R. The PCR reactions were performed using 10 ng of DNA, 0.5
546 µM primers, 0.2 mM dNTP, and 0.5 U of the DNA-free Taq-polymerase, MolTaq 16S
547 DNA Polymerase (Molzym). The amplifications were carried out using the following
548 profile: 1 cycle at 94°C for 60 s, followed by 30 cycles at 94°C for 60 s, 65°C for 60 s,
549 72°C for 60 s, and finishing with a step at 72°C for 10 min. The PCR reactions were
550 sent to the @Bridge platform (INRAe, Jouy-en-Josas) for sequencing using Illumina
551 Miseq technology. Single multiplexing was performed using home-made 6 bp index,
552 which were added to R784 during a second PCR with 12 cycles using forward primer
553 (AATGATACGGCGACCACCGAGATCTACACTCTTTCCCTACACGAC) and reverse
554 primer(CAAGCAGAAGACGGCATACGAGAT-index
555 GTGACTGGAGTTCAGACGTGT). The resulting PCR products were purified and
556 loaded onto the Illumina MiSeq cartridge according to the manufacturer instructions.
557 The quality of the run was checked internally using PhiX, and then, sequences were
558 assigned to its sample with the help of the previously integrated index. High quality
559 filtered reads were further assembled and processed using FROGS pipeline (Find
560 Rapidly OTU with Galaxy Solution) to obtain OTUs and their respective taxonomic
561 assignment thanks to Galaxy instance (https://migale.inra.fr/galaxy). In each dataset,
562 more than 97% of the paired-end sequences were assembled using at least a 10-bp
563 overlap between the forward and reverse sequences. The following successive steps
564 involved de-noising and clustering of the sequences into OTUs using SWARM,
565 chimera removal using VSEARCh. Then, cluster abundances were filtered at
566 0.005%. One hundred percent of clusters were affiliated to OTU by using a silva138
567 16S reference database and the RDP (Ribosomal Database Project) classifier
568 taxonomic assignment procedure. Richness and diversity indexes of bacterial
569 community, as well as clustering and ordinations, were computed using the Phyloseq
570 package (v 1.19.1) in RStudio software[57]. Divergence in community composition
571 between samples was quantitatively assessed by calculating β-diversity index
572 (UniFrac and weighted UniFrac distance matrices). For the heatmap, a negative
573 binomial model was fit to each OTU, using DESeq2[50] with default parameters, to
574 estimate abundance log-fold changes (FCs). Values of *P* were corrected for multiple
575 testing using the Benjamini-Hochberg procedure to control the false-discovery rate
576 and significant OTUs were selected based on effect size (FC >|2|, adjusted *P* value
577 <0.05).

578 **Mass spectrometry**
579 *Protein digestion*
580 Immunoprecipitation eluates were digested following a FASP protocol[58] slightly
581 modified. Briefly, proteins were reduced using 100 mM DTT (dithiothreitol) for 1h at
582 60°C. Proteins were alkylated for 30 min by incubation in the dark at room
583 temperature with 100 µL of 50 mM iodoacetamide. Samples were digested with 2µL
584 of sequencing grade modified trypsin (Promega, WI, USA) for 16h at 37°C. Peptides
585 were collected by centrifugation at 15,000 x g for 10 min followed by one wash with
586 50mM ammonium bicarbonate and vacuum dried.
587 *NanoLC-MS/MS protein identification and quantification*
588 Peptides were resuspended in 21 µL of 10% ACN, 0.1% TFA in HPLC-grade water
589 prior MS analysis. For each run, 5 µL were injected in a nanoRSLC-Q Exactive PLUS
590 (RSLC Ultimate 3000) (Thermo Scientific,Waltham MA, USA). Peptides were loaded
591 onto a µ-precolumn (Acclaim PepMap 100 C18, cartridge, 300 µm i.d.×5 mm, 5 µm)
592 (Thermo Scientific), and were separated on a 50 cm reversed-phase liquid
593 chromatographic column (0.075 mm ID, Acclaim PepMap 100, C18, 2 µm) (Thermo
594 Scientific). Chromatography solvents were (A) 0.1% formic acid in water, and (B)
595 80% acetonitrile, 0.08% formic acid. Peptides were eluted from the column with the
596 following gradient 5% to 40% B (38 minutes), 40% to 80% (1 minute). At 39 minutes,
597 the gradient stayed at 80% for 4 minutes and, at 43 minutes, it returned to 5% to re-
598 equilibrate the column for 16 minutes before the next injection. Two blanks were run
599 between each series to prevent sample carryover. Peptides eluting from the column
600 were analyzed by data dependent MS/MS, using top-10 acquisition method. Peptides
601 were fragmented using higher-energy collisional dissociation (HCD). Briefly, the
602 instrument settings were as follows: resolution was set to 70,000 for MS scans and
603 17,500 for the data dependent MS/MS scans in order to increase speed. The MS
604 AGC target was set to 3.10^6 counts with maximum injection time set to 200 ms, while
605 MS/MS AGC target was set to 1.10^5 with maximum injection time set to 120 ms. The
606 MS scan range was from 400 to 2000 m/z.
607 *Data Analysis following nanoLC-MS/MS acquisition*
608 Raw files corresponding to the proteins immunoprecipitated were analyzed using
609 MaxQuant 1.5.5.1 software against the Human Uniprot KB/Swiss-Prot database
610 2016-01 [59]. To search parent mass and fragment ions, we set a mass deviation of 3
611 ppm and 20 ppm respectively, no match between runs allowed.
612 Carbamidomethylation (Cys) was set as fixed modification, whereas oxidation (Met)
613 and N-term acetylation were set as variable modifications. The false discovery rates
614 (FDRs) at the protein and peptide level were set to 1%. Scores were calculated using
615 MaxQuant as described previously[59]. Peptides were quantified according to the
616 MaxQuant MS1 signal intensities. Statistical and bioinformatic analysis, including
617 volcano plot, were performed with Perseus software version 1.6.7.0 (freely available
618 at www.perseus-framework.org). For statistical comparison, we set two groups, IP
619 and negative control, each containing 3 biological replicates. We then retained only
620 proteins that were quantified 3 times in at least one group. Next, the data were
621 imputed to fill missing data points by creating a Gaussian distribution of random

numbers with a standard deviation of 33% relative to the standard deviation of the measured values and 3 standard deviation downshift of the mean to simulate the distribution of low signal values. We performed a T-test, and represented the data on a volcano plot (FDR<0.05, S0=1).

SDS-PAGE and immunoblotting

Intestinal epithelial cells purified from mice (at least n = 3 separate experiments) were lysed at 4 °C in a buffer containing 25mM Tris pH 7.5, 1mM EDTA, 0.1mM EGTA, 5mM $MgCl_2$, 1% NP-40, 10% Glycerol, 150mM NaCl, and then cleared by centrifugation at 14,000 rpm for 30 min at 4 °C. Proteins were separated on SDS–PAGE gels and transferred to nitrocellulose membranes by standard procedures. Mouse anti-progerin monoclonal antibody (13A4DA, sc-81611, Santa Cruz), anti-HP1 α (2H4E9, Novus Biologicals), HP1 β (1MOD-1A9, Thermo Scientific) and HP1 γ (2MOD-IG6, Thermo Scientific) and γ Tubulin (4D11, Thermo Scientific) antibodies.

Statistical Analyses

Statistical analyses were performed with the GraphPad Prism soft-ware. Differences between groups were assayed using a two-tailed Student's t-test using GraphPad Prism. In all cases, the experimental data were assumed to fulfill t-test requirements (normal distribution and similar variance); in those cases, where the assumption of the t-test was not valid, a nonparametric statistical method was used (Mann–Whitney test). The differences between three or more groups were tested by one-way ANOVA. A p-value less than 0.05 was considered as significant. Error bars indicate the standard error of the mean.

Data access

RNA-seq data, the derived mm9.bigwig files, and the *de novo* junction.bed files generated in this study have been submitted to the NCBI Gene Expression Omnibus (GEO; http://www.ncbi.nlm.nih.gov/geo/) under accession numbers GSE192800. **Access will be granted to reviewers with the following token: mdkrywoyphyplwh**

ACKNOWLEDGMENTS

We thank Florence Cammas for providing the *Cbx3*$^{fl/fl}$ mice. We thanks Dr Zhou Zhongjun (Department of Biochemistry, Li Ka Shing Faculty of Medicine The university of Hong Kong) for providing us MEF from HGPS mice. We thank Dr Cohen-Tannoudji for providing the Villin-CreERT2 mice (Institut Pasteur, Paris, France)

FUNDINGS

This work has been supported by the «Agence National de la Recherche» (ANR) grant (EPI-CURE, R16154KK).

BIBLIOGRAPHY

1. Annese, V. Genetics and epigenetics of IBD. *Pharmacol Res* **159,** 104892 (2020).
2. Allshire, R. C. & Madhani, H. D. Ten principles of heterochromatin formation

663 and function. *Nat Rev Mol Cell Biol* **19,** 229–244 (2018).
664 3. Casale, A. M., Cappucci, U., Fanti, L. & Piacentini, L. Heterochromatin protein
665 1 (HP1) is intrinsically required for post-transcriptional regulation of Drosophila
666 Germline Stem Cell (GSC) maintenance. *Sci Rep* **9,** 4372–12 (2019).
667 4. Rachez, C. *et al.* HP1γ binding pre-mRNA intronic repeats modulates RNA
668 splicing decisions. *EMBO Rep.* **22,** e52320 (2021).
669 5. Saint-André, V., Batsche, E., Rachez, C. & Muchardt, C. Histone H3 lysine 9
670 trimethylation and HP1γ favor inclusion of alternative exons. *Nat. Struct. Mol.*
671 *Biol.* **18,** 337–344 (2011).
672 6. Smallwood, A. *et al.* CBX3 regulates efficient RNA processing genome-wide.
673 *Genome Res.* **22,** 1426–1436 (2012).
674 7. Scotti, M. M. & Swanson, M. S. RNA mis-splicing in disease. *Nat Rev Genet* **17,**
675 19–32 (2016).
676 8. Harouz, H. *et al.* Shigella flexneri targets the HP1γ subcode through the
677 phosphothreonine lyase OspF. *EMBO J.* **33,** 2606–2622 (2014).
678 9. Tréton, X. *et al.* Combined NADPH oxidase 1 and interleukin 10 deficiency
679 induces chronic endoplasmic reticulum stress and causes ulcerative colitis-like
680 disease in mice. *PLoS ONE* **9,** e101669 (2014).
681 10. Lee, Y.-H. & Ann, D. K. Bi-phasic expression of Heterochromatin Protein 1
682 (HP1) during breast cancer progression: Potential roles of HP1 and chromatin
683 structure in tumorigenesis. *J Nat Sci* **1,** e127 (2015).
684 11. Fan, Y., Li, H., Liang, X. & Xiang, Z. CBX3 promotes colon cancer cell
685 proliferation by CDK6 kinase-independent function during cell cycle.
686 *Oncotarget* **8,** 19934–19946 (2017).
687 12. Oyama, K. *et al.* Deletion of HP1γ in cardiac myocytes affects H4K20me3
688 levels but does not impact cardiac growth. *Epigenetics Chromatin* **11,** 18–15
689 (2018).
690 13. Zeng, M. Y., Inohara, N. & Nuñez, G. Mechanisms of inflammation-driven
691 bacterial dysbiosis in the gut. *Mucosal Immunol* **10,** 18–26 (2017).
692 14. Greuter, T. *et al.* Gender Differences in Inflammatory Bowel Disease. *Digestion*
693 **101 Suppl 1,** 98–104 (2020).
694 15. Halfvarson, J. *et al.* Dynamics of the human gut microbiome in inflammatory
695 bowel disease. *Nat Microbiol* **2,** 17004–7 (2017).
696 16. Nielsen, S. J. *et al.* Rb targets histone H3 methylation and HP1 to promoters.
697 *Nature* **412,** 561–565 (2001).
698 17. Carroll, T. D., Newton, I. P., Chen, Y., Blow, J. J. & Näthke, I. Lgr5+ intestinal
699 stem cells reside in an unlicensed G1 phase. *J. Cell Biol.* **217,** 1667–1685
700 (2018).
701 18. Altmann, G. G. A gradual decrease in nucleolar size with the maturation of
702 columnar epithelial cells in the adult rat intestine under normal and various
703 experimental conditions. *J. Cell. Sci.* **77,** 289–304 (1985).
704 19. Ameyar-Zazoua, M. *et al.* Argonaute proteins couple chromatin silencing to
705 alternative splicing. *Nat. Struct. Mol. Biol.* **19,** 998–1004 (2012).
706 20. Wan, Y. & Larson, D. R. Splicing heterogeneity: separating signal from noise.
707 *Genome Biol* **19,** 86–10 (2018).
708 21. Chen, L., Tovar-Corona, J. M. & Urrutia, A. O. Increased levels of noisy
709 splicing in cancers, but not for oncogene-derived transcripts. *Human Molecular*
710 *Genetics* **20,** 4422–4429 (2011).
711 22. Yoshida, K. *et al.* Frequent pathway mutations of splicing machinery in
712 myelodysplasia. *Nature* **478,** 64–69 (2011).

713 23. Tan, Q. *et al.* Extensive cryptic splicing upon loss of RBM17 and TDP43 in
714 neurodegeneration models. *Human Molecular Genetics* **25,** 5083–5093 (2016).
715 24. Humphrey, J., Emmett, W., Fratta, P., Isaacs, A. M. & Plagnol, V. Quantitative
716 analysis of cryptic splicing associated with TDP-43 depletion. *BMC Med*
717 *Genomics* **10,** 38–17 (2017).
718 25. Sun, X. *et al.* Intestinal epithelial PKM2 serves as a safeguard against
719 experimental colitis via activating β-catenin signaling. *Mucosal Immunol* **12,**
720 1280–1290 (2019).
721 26. Sharma, S., Liao, W., Zhou, X., Wong, D. T. W. & Lichtenstein, A. Exon 11
722 skipping of E-cadherin RNA downregulates its expression in head and neck
723 cancer cells. *Mol Cancer Ther* **10,** 1751–1759 (2011).
724 27. Eriksson, M. *et al.* Recurrent de novo point mutations in lamin A cause
725 Hutchinson-Gilford progeria syndrome. *Nature* **423,** 293–298 (2003).
726 28. Scaffidi, P. & Misteli, T. Lamin A-dependent nuclear defects in human aging.
727 *Science* **312,** 1059–1063 (2006).
728 29. Vautrot, V. *et al.* Enhanced SRSF5 Protein Expression Reinforces Lamin A
729 mRNA Production in HeLa Cells and Fibroblasts of Progeria Patients. *Hum*
730 *Mutat* **37,** 280–291 (2016).
731 30. Dong, Y., Cirimotich, C. M., Pike, A., Chandra, R. & Dimopoulos, G. Anopheles
732 NF-κB-regulated splicing factors direct pathogen-specific repertoires of the
733 hypervariable pattern recognition receptor AgDscam. *Cell Host Microbe* **12,**
734 521–530 (2012).
735 31. Hattori, D. *et al.* Robust discrimination between self and non-self neurites
736 requires thousands of Dscam1 isoforms. *Nature* **461,** 644–648 (2009).
737 32. Pickrell, J. K., Pai, A. A., Gilad, Y. & Pritchard, J. K. Noisy splicing drives
738 mRNA isoform diversity in human cells. *PLoS Genet.* **6,** e1001236 (2010).
739 33. Hsieh, Y.-C. *et al.* Tau-Mediated Disruption of the Spliceosome Triggers
740 Cryptic RNA Splicing and Neurodegeneration in Alzheimer's Disease. *Cell Rep*
741 **29,** 301–316.e10 (2019).
742 34. Fong, L. G. *et al.* Activating the synthesis of progerin, the mutant prelamin A in
743 Hutchinson-Gilford progeria syndrome, with antisense oligonucleotides. *Human*
744 *Molecular Genetics* **18,** 2462–2471 (2009).
745 35. Liu, G.-H. *et al.* Recapitulation of premature ageing with iPSCs from
746 Hutchinson-Gilford progeria syndrome. *Nature* **472,** 221–225 (2011).
747 36. Keller, C. *et al.* HP1(Swi6) mediates the recognition and destruction of
748 heterochromatic RNA transcripts. *Mol. Cell* **47,** 215–227 (2012).
749 37. Eissenberg, J. C. *et al.* Mutation in a heterochromatin-specific chromosomal
750 protein is associated with suppression of position-effect variegation in
751 Drosophila melanogaster. *Proc. Natl. Acad. Sci. U.S.A.* **87,** 9923–9927 (1990).
752 38. Motamedi, M. R. *et al.* HP1 proteins form distinct complexes and mediate
753 heterochromatic gene silencing by nonoverlapping mechanisms. *Mol. Cell* **32,**
754 778–790 (2008).
755 39. Sanulli, S. *et al.* HP1 reshapes nucleosome core to promote phase separation
756 of heterochromatin. *Nature* **575,** 390–394 (2019).
757 40. Larson, K. *et al.* Heterochromatin formation promotes longevity and represses
758 ribosomal RNA synthesis. *PLoS Genet.* **8,** e1002473 (2012).
759 41. Jeon, H.-J. *et al.* Effect of heterochromatin stability on intestinal stem cell aging
760 in Drosophila. *Mech Ageing Dev* **173,** 50–60 (2018).
761 42. Zhang, W. *et al.* Aging stem cells. A Werner syndrome stem cell model unveils
762 heterochromatin alterations as a driver of human aging. *Science* **348,** 1160–

763 1163 (2015).
764 43. Shumaker, D. K. *et al.* Mutant nuclear lamin A leads to progressive alterations
765 of epigenetic control in premature aging. *Proc. Natl. Acad. Sci. U.S.A.* **103,**
766 8703–8708 (2006).
767 44. Scaffidi, P. & Misteli, T. Lamin A-dependent misregulation of adult stem cells
768 associated with accelerated ageing. *Nat. Cell Biol.* **10,** 452–459 (2008).
769 45. Häsler, R. *et al.* Alterations of pre-mRNA splicing in human inflammatory bowel
770 disease. *Eur J Cell Biol* **90,** 603–611 (2011).
771 46. Häsler, R. *et al.* Uncoupling of mucosal gene regulation, mRNA splicing and
772 adherent microbiota signatures in inflammatory bowel disease. *Gut* **66,** 2087–
773 2097 (2017).
774 47. Berger, K., Somineni, H., Prince, J., Kugathasan, S. & Gibson, G. Altered
775 splicing associated with the pathology of inflammatory bowel disease. *Hum*
776 *Genomics* **15,** 47–10 (2021).
777 48. Le Gallou, S., Nojima, T., Kitamura, D., Weill, J.-C. & Reynaud, C.-A. The AID-
778 Cre-ERT2 Model: A Tool for Monitoring B Cell Immune Responses and
779 Generating Selective Hybridomas. *Methods Mol Biol* **1623,** 243–251 (2017).
780 49. Nigro, G., Hanson, M., Fevre, C., Lecuit, M. & Sansonetti, P. J. Intestinal
781 Organoids as a Novel Tool to Study Microbes-Epithelium Interactions. *Methods*
782 *Mol Biol* **1576,** 183–194 (2019).
783 50. Love, M. I., Huber, W. & Anders, S. Moderated estimation of fold change and
784 dispersion for RNA-seq data with DESeq2. *Genome Biol* **15,** 550–21 (2014).
785 51. Shen, S. *et al.* rMATS: robust and flexible detection of differential alternative
786 splicing from replicate RNA-Seq data. *Proc. Natl. Acad. Sci. U.S.A.* **111,**
787 E5593–601 (2014).
788 52. Ramírez, F. *et al.* deepTools2: a next generation web server for deep-
789 sequencing data analysis. *Nucleic Acids Res* **44,** W160–5 (2016).
790 53. Yeo, G. & Burge, C. B. Maximum entropy modeling of short sequence motifs
791 with applications to RNA splicing signals. *J Comput Biol* **11,** 377–394 (2004).
792 54. Quinlan, A. R. & Hall, I. M. BEDTools: a flexible suite of utilities for comparing
793 genomic features. *Bioinformatics* **26,** 841–842 (2010).
794 55. Muñoz, J. *et al.* The Lgr5 intestinal stem cell signature: robust expression of
795 proposed quiescent '+4' cell markers. *EMBO J.* **31,** 3079–3091 (2012).
796 56. Haber, A. L. *et al.* A single-cell survey of the small intestinal epithelium. *Nature*
797 **551,** 333–339 (2017).
798 57. McMurdie, P. J. & Holmes, S. Phyloseq: a bioconductor package for handling
799 and analysis of high-throughput phylogenetic sequence data. *Pac Symp*
800 *Biocomput* 235–246 (2012).
801 58. Lipecka, J. *et al.* Sensitivity of mass spectrometry analysis depends on the
802 shape of the filtration unit used for filter aided sample preparation (FASP).
803 *Proteomics* **16,** 1852–1857 (2016).
804 59. Cox, J. & Mann, M. MaxQuant enables high peptide identification rates,
805 individualized p.p.b.-range mass accuracies and proteome-wide protein
806 quantification. *Nat Biotechnol* **26,** 1367–1372 (2008).
807